

AD-A119 583

WESTINGHOUSE RESEARCH AND DEVELOPMENT CENTER PITTSBU--ETC F/G 20/5
EXCITATION OF MERCURIC BROMIDE BY ELECTRONS.(U)

AUG 82 P J CHANTRY, C L CHEN

N00014-81-C-0518

UNCLASSIFIED

82-9C1-EXCIT-R1

NL

1 0+ |
ADA
18 583

END

DATE

FILED

DTIC

EXCITATION OF MERCURIC BROMIDE BY ELECTRONS

12 6

AD A119583

P. J. Chantry and C. L. Chen

FINAL REPORT

For Period of May 15, 1981, to June 30, 1982

Sponsored by
Office of Naval Research

Monitored by
Office of Naval Research

August 30, 1982

DTIC
ELECTE
SEP 27 1982
F

DTIC FILE COPY

This document has been approved
for public release and sale; its
distribution is unlimited.



Westinghouse R&D Center
1310 Beulah Road
Pittsburgh, Pennsylvania 15235

82 01 00 000

EXCITATION OF MERCURIC BROMIDE BY ELECTRONS

P. J. Chantry and C. L. Chen

FINAL REPORT

For Period of May 15, 1981, to June 30, 1982

Sponsored by
Office of Naval Research

Monitored by
Office of Naval Research

August 30, 1982



Westinghouse R&D Center
1310 Beulah Road
Pittsburgh, Pennsylvania 15235

Unclassified

SECURITY CLASSIFICATION OF THIS PAGE (When Data Entered)

REPORT DOCUMENTATION PAGE		READ INSTRUCTIONS BEFORE COMPLETING FORM
1. REPORT NUMBER 82-9C1-EXCIT-RI	2. GOVT ACCESSION NO. AD A119583	3. RECIPIENT'S CATALOG NUMBER
4. TITLE (and Subtitle) Excitation of Mercuric Bromide by Electrons		5. TYPE OF REPORT & PERIOD COVERED Final Report 5/15/81 - 6/30/82
		6. PERFORMING ORG. REPORT NUMBER
7. AUTHOR(s) P. J. Chantry and C. L. Chen		8. CONTRACT OR GRANT NUMBER(s) N00014-81-C-0518
9. PERFORMING ORGANIZATION NAME AND ADDRESS Westinghouse R&D Center 1310 Beulah Road Pittsburgh, PA 15235		10. PROGRAM ELEMENT, PROJECT, TASK AREA & WORK UNIT NUMBERS
11. CONTROLLING OFFICE NAME AND ADDRESS Office of Naval Research 800 North Quincy Street Arlington, VA 22217		12. REPORT DATE August 30, 1982
		13. NUMBER OF PAGES 56
14. MONITORING AGENCY NAME & ADDRESS (if different from Controlling Office)		15. SECURITY CLASS. (of this report) Unclassified
		15a. DECLASSIFICATION/DOWNGRADING SCHEDULE
16. DISTRIBUTION STATEMENT (of this Report) Approved for public release; distribution unlimited.		
17. DISTRIBUTION STATEMENT (of the abstract entered in Block 20, if different from Report)		
18. SUPPLEMENTARY NOTES		
19. KEY WORDS (Continue on reverse side if necessary and identify by block number) Mercuric Bromide, Dissociation, Emission, Fluorescence, Cross Sections, Electron, Impact, Beams, Laser, Excitation.		
20. ABSTRACT (Continue on reverse side if necessary and identify by block number) Computer modelling of the HgBr discharge laser requires as input the various cross sections for electron impact on HgBr ₂ . One of the most important of these is the cross section for production of the HgBr* (B ² Σ _{1/2}), the upper laser state, by electron impact on HgBr ₂ . This report describes work performed to measure the total emission cross section for production of the HgBr B-X fluorescence. Under the conditions of the experiment this corresponds to the total formation cross section for the HgBr*(B) state. A		

DD FORM 1 JAN 73 1473

EDITION OF 1 NOV 65 IS OBSOLETE
S. N. 0102-LF-014-6601

Unclassified

SECURITY CLASSIFICATION OF THIS PAGE (When Data Entered)

Unclassified

SECURITY CLASSIFICATION OF THIS PAGE (When Data Entered)

20. Cont'd.

magnetically collimated electron beam (1-200 eV) crosses a low density molecular beam of HgBr_2 . The apparatus permits simultaneous measurements of negative ion, positive ion, and wavelength resolved photon production from HgBr_2 , and from permanent bottled gases. The relative wavelength dependence of the photon counting system has been determined from 280 to 640 nm using standard lamps. By comparison with known ionization and total emission cross sections in He it is possible to measure total emission cross sections for other molecules whose ionization cross sections are known. The $\text{HgBr}^*(\text{B})$ emission extends from 510 nm to beyond 350 nm, and appropriate integration over wavelength is necessary. The resulting cross section has a sharp onset at 6.0 eV and rises rapidly to a plateau with a mean value of $3.2 (-16) \text{ cm}^2$. In the region (3-5 eV) of dissociative attachment $\text{HgBr}^*(\text{B})$ production is undetectable, corresponding to $\sigma < (-18) \text{ cm}^2$.

Accession For	
DTIS GRA&I	<input checked="" type="checkbox"/>
DTIC TAB	<input type="checkbox"/>
Unannounced	<input type="checkbox"/>
Justification	
By	
Distribution/	
Availability Codes	
Dist	Avail and/or Special
A	

2
COPY
INSPECTED

5 N 0102-LF-014-6601

Unclassified

SECURITY CLASSIFICATION OF THIS PAGE(When Data Entered)

Contents

	<u>Page</u>
1. SUMMARY	1
1.1 Objectives and Approach	1
1.2 Accomplishments	1
1.3 Suggested Further Work	2
2. INTRODUCTION	4
3. EXPERIMENT	8
3.1 General Approach	8
3.2 Electrode Structure	9
3.3 Molecular Beam Head and Material Handling Systems	10
3.4 Photon Counting System	13
3.5 Data Analysis	16
4. RESULTS	20
4.1 Wavelength Dependence of the Quantum Detection Efficiency	20
4.2 Helium Line Calibration Data	22
4.3 Ion Collection Efficiencies	24
4.4 Measurements in HgBr ₂	26
5. DISCUSSION	31

1. SUMMARY

1.1 Objectives and Approach

The objectives of the present contract were to (i) modify an existing apparatus to allow use of HgBr_2 as the study gas, and (ii) to measure the shape and absolute magnitude of the total cross section for production of the $\text{HgBr}^*(B^2\Sigma_{1/2})$ state by electron impact on HgBr_2 .

A magnetically collimated electron beam (1-200 eV) is crossed by a molecular beam of HgBr_2 . The apparatus permits simultaneous measurements of negative ion, positive ion, and wavelength resolved photon production from HgBr_2 . Equivalent measurements can also be made for reference permanent gases. Helium is used for this purpose since a number of line emission cross sections in the relevant wavelength region have been accurately measured by Van Zyl et al. (1980). This method of calibrating the apparatus makes it possible to measure the ratio of the emission cross section to the total ionization cross section for any other gas, provided the wavelength dependence of the relative quantum efficiency of the optical detection system and the relative ion collection efficiency are known.

1.2 Accomplishments

The material handling system developed for HgBr_2 involves a sealed capsule of the powder within the system on assembly. When desired the capsule is cracked open by a bellows sealed plunger, and thereafter the transport of the HgBr_2 is controlled by a system of heaters, and a reservoir cooler. This system has proven to be trouble-free and allows very close control of the HgBr_2 vapor pressure and consequent molecular beam intensity.

The relative quantum efficiency of the photon counting system has been measured over the range 240-650 nm, using two standard lamps to cover the range. Good agreement is achieved in the region of overlap.

Helium reference calibration data has been taken at a number of lines, including the (4^1S-2^1P) transition at 504.8 nm, the (5^1S-2^1P) at 443.8 nm, and the (6^1S-2^1P) at 416.9 nm. The line emission cross sections for these have been carefully measured by Van Zyl et al. (1980), and they form the basis for calibrating the present system. Overall, very good consistency was achieved between the present measurements of these lines, the independently measured relative quantum efficiencies at the three wavelengths, and the dependence of the cross sections on electron energy reported by Van Zyl et al.

The measured $HgBr^*(B-X)$ emission spectrum extends from ~ 510 nm to shorter wavelengths, depending on the electron energy. Above ~ 10 eV it extends to ~ 300 nm, and has a shape which is relatively insensitive to energy at higher energies. The threshold has been measured to be at 6.0 ± 0.1 eV, the appearance curve for positive ions being used for electron energy scale calibration. The total emission cross section, measured at a number of electron energies by suitable integration of the measured continuum, rises rapidly from threshold to a plateau value of $3.2 \times 10^{-16} \text{ cm}^2$ above ~ 9 eV.

Previous workers (Degani et al. 1981) have suggested that $HgBr^*(B)$ state production accompanies Br^- formation by dissociative attachment, in the 3-5 eV region. Other workers (Nygaard, 1981) have reported evidence for such a process, from fluorescence measurements in a drift tube. In the present experiment we find no such evidence, and conclude that the cross section for such a process must be less than 10^{-18} cm^2 in this energy range.

All the objectives of the present contract were met.

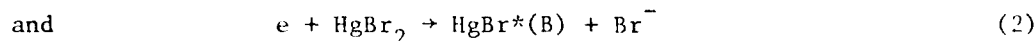
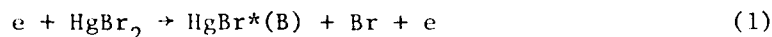
1.3 Suggested Further Work

Using the present apparatus it would be possible to measure a number of additional cross sections in $HgBr_2$, and thereby further reduce the uncertainties remaining in the basic data used as input for laser modelling calculations. Based on the cross section measured in the present work modifications have already been found necessary in the

assumed shapes and magnitudes of the other inelastic cross sections (Kline et al., 1982). Additional crossed beam measurements using the trapped electron technique would allow confirmation of the various thresholds, and provide estimates of the rate of rise of these cross sections with energy above threshold. Further, using optical detection techniques, as in the present experiment, a measurement could be made of the shape and magnitude of the total formation cross section of the $\text{HgBr}^*(C)$ state from HgBr_2 .

2. INTRODUCTION

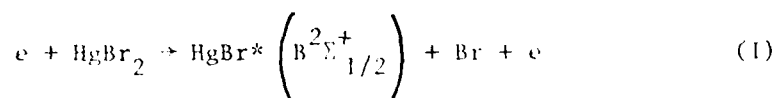
The objectives of the present program were (i) to modify an existing apparatus to allow the measurement of electron impact excitation of metal halides and (ii) to measure the cross section for production of the $\text{HgBr}^*(B)$ state by dissociative excitation of HgBr_2 . Two possible such reactions are



These measurements were to be performed over the energy range 1 to 100 eV, with particular emphasis on the region below 30 eV where serious discrepancies exist between a previous measurement (Allison & Zare, 1978) and estimates based on Boltzmann Code modelling of swarm and discharge experiments (Nighan, Hinchey & Wiegand, 1982; Hsia, McGeoch and Klimek, 1981). A quantitative knowledge of this process is vital to on-going efforts to model the discharge and laser kinetics of the HgBr laser system.

Laser action on the $B^2\Sigma^+_{1/2} \rightarrow X^2\Sigma^+_{1/2}$ band of HgBr at 502 nm has been observed independently by several investigators (Parks, 1977; Schimitschek et al, 1977). This bound-bound laser transition originates on the first excited electronic state, $B^2\Sigma^+_{1/2}$, of the HgBr molecule at $v' = 0$, and terminates on the $X^2\Sigma^+_{1/2}$ state at $v'' = 22$. The large Franck-Condon shift of the $B \rightarrow X$ states suggests that for pulsed excitation, bottlenecking of the lower laser level is minimal given rapid deactivation of the X state $v'' = 22$ level through collisional quenching at high buffer gas pressures. Thus, the HgBr laser, emitting at 502 nm, appears to be promising as a source for high power, high efficiency laser radiation in the blue-green region of the spectrum.

The upper laser level can be produced by dissociative excitation of HgBr_2 by photons (Schimitschek et al, 1977), by excitation transfer from electronically excited neutrals (Chang & Burnham, 1980), or by electron impact (Allison & Zare, 1978). The latter two processes are particularly important in electric discharge pumped lasers, and quantitative data are essential to any attempt to properly model (Nighan et al., 1982; Hsia et al., 1981) the discharge and laser kinetics of such devices. The present program provides quantitative data on the cross section for electron impact dissociative excitation of HgBr_2 :

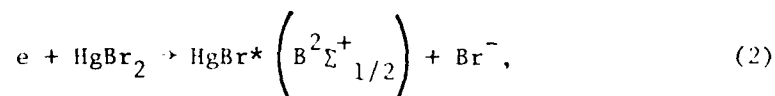


and places an upper limit on the cross section for Reaction (2).

The importance of reaction (1) in laser discharges is now generally recognized, but this has not always been the case. The initial success of a discharge pumped laser (Schimitschek and Celto, 1978) was ascribed to this reaction, but when the cross section reported by Allison and Zare (1978) was used in subsequent modelling studies (Nighan, 1980), it was concluded that this reaction was relatively unimportant compared to the excitation exchange reactions. Unfortunately, complete confidence cannot be placed in the cross section for reaction (1) reported by Allison and Zare (1978), particularly in the important low energy region. Because of the type of electron gun employed, these authors were not able to make measurements in the threshold region immediately above 6 eV. The measurements performed in the region of 20 eV, where the electron gun's performance was becoming inadequate, indicated that the cross section was decreasing rapidly with decreasing energy, with an apparent threshold at ~ 25 eV. This result is surprising in view of the known states of HgBr_2^* in the region below 10 eV, at least one of which dissociates to form $\text{HgBr}(B^2\Sigma^+_{1/2})$, and is accessible optically. Consequently, in subsequent laser modelling efforts (Hsia et al., 1981; Nighan et al., 1982), this cross section has been treated as an adjustable input with the constraint that the threshold be consistent with the optical absorption data of

Wieland (1932), and the inelastic scattering spectrum of Spence and Dillon (1981). Most workers have assumed a 6.4 eV threshold.

In this situation it was clearly desirable to remeasure the cross section for reaction (1), with particular emphasis on the low energy region, below 30 eV. An additional incentive for doing so arises from the work of Degani, Rokni, and Yatsiv (1981) who proposed that the $\text{HgBr}^*(\text{B})$ state is also produced by the dissociative attachment reaction:



Subsequent measurement of the cross section for Br^- production, by Wiegand and Boedeker (1982), is consistent with this proposal in that the measured threshold for Br^- production is very close to that predicted for reaction (2). However, Nighan et al (1982) have recently concluded that only a small fraction, if any, of the dissociative attachment process can be accompanied by $\text{HgBr}^*(\text{B})$ state production. In order to address this question it has been necessary to perform measurements at energies well below the ~ 6 eV threshold anticipated for reaction (1). In the present experiment the use of a magnetically collimated electron beam has allowed measurements to be made at energies well below 1 eV, allowing both reactions (1) and (2) to be fully explored.

The interaction of an electron with an isolated atom or molecule can lead to production of a particular excited state either directly, or indirectly through radiative cascade from higher levels optically coupled to the state in question. The cross section for direct production of a particular state is referred to as the "excitation cross section". This cross section can be obtained from measurements of all the radiation originating from the level of interest, provided proper account is taken of the indirect cascade contribution. The latter may involve a number of higher states, and may not be possible to do with accuracy.

Measurement of the radiation produced by a particular electronic transition leads directly to an estimate of the "emission cross section". In the simplest, two-level system this is identical to the excitation cross section. Formation of the upper state indirectly by cascade tend to make the emission cross section larger than the excitation cross section, while branching from the upper state to multiple lower states tends to do the opposite.

For purposes of laser discharge modelling one would like to know both the excitation cross section and the total B state formation cross section. The former is the proper cross section for representing the energy lost inelastically by the electrons in direct excitation of the B state. The latter allows the total formation rate of the B state to be calculated. In the present work we have measured the total (and wavelength resolved) emission cross section for the production of the B-X radiation. Since the B state is radiatively coupled to only one lower state (X) this corresponds to the total B state formation cross section.

3. EXPERIMENT

3.1 General Approach

The various problems attending the measurement of an independent absolute emission cross section are discussed in detail in the excellent paper by Van Zyl et al. (1980). Two aspects of such a measurement present particularly difficult problems in the present context - (i) the measurement of the absolute number density of the HgBr_2 molecules in the interaction region, and (ii) the absolute calibration of the optical detection system. In the present work we avoid many of these difficulties by (i) using measurements of the positive ions produced in the interaction region as a measure of the neutral gas number density and (ii) using emission measurements in Helium to calibrate the optical detection system, using particularly the "benchmark" emission cross sections determined by Van Zyl et al. (1980). In addition the relative wavelength dependence of the optical detection system is determined using two standard (deuterium and quartz halogen) lamps to cover the wavelength range of interest (300-600 nm).

The configuration of the experiment is represented schematically in Figure 1. The gas under study is introduced into the collision region in the form of a molecular beam, directed vertically downward into the throat of a liquid nitrogen cooled baffle, placed above an oil diffusion pump. A magnetically collimated electron beam travels perpendicularly through the molecular beam such that they interact in the central region of a "collision chamber". In a direction orthogonal to both beams the interaction region is viewed through aligned slits in the ion repeller plate and the containing box, which together with the ion attractor plate constitute the collision chamber. The interaction region is focussed on the entrance slit of a grating monochromator whose exit slit is focussed on the photocathode of a cooled photomultiplier operated as a photon counter.

The "ion attractor" and "ion repeller" electrodes shown in Figure 1 are electrically isolated parallel plates mounted within the collision chamber. By appropriately biasing these electrodes relative to the collision chamber box it is possible to collect and measure both positive and negative ions produced by the interaction of the crossed electron and molecular beams. Details of the various components are described below under separate sub-headings.

3.2 Electrode Structure

The structure of the electron gun, the collision chamber, and the electron collector is shown to scale in Figure 2. Electrode 1 is typically set between a few volts and ten volts positive relative to the thorium-coated iridium filament, such that the emission is temperature controlled. Electrode 3 is normally operated slightly negative relative to the filament, and provides voltage control of the electron current transmitted to the collision chamber. It also serves as the retarding electrode when the gun is operated in the "Retarding Potential Difference" (RPD) mode (Fox et al., 1955; Chantry, 1969). Electrodes 2 and 4 provide electrostatic shielding of electrode 3. The electron beam enters the collision chamber through aperture 5A and leaves through aperture 5B. The electron collector (7) is normally biased positive relative to aperture 6, which in turn is normally biased positive relative to the collision chamber. Plate 7A is held at the same potential as the electron collector and functions as a "guard" for electron current measurements. Transmitted currents of a few $\times 10^{-5}$ A or less were routinely used. No deterioration of the filament performance was observed in the presence of HgBr_2 .

The "ion attractor" and "ion repeller" plates are electrically isolated from the surrounding collision chamber box and are normally biased sufficiently to collect a large fraction of the ions, positive and negative, respectively, formed at the intersection region of the electron and molecular beams. The centrally located rectangles shown in Figure 2 represent the apertures in the top and bottom of the collision chamber. The smaller aperture in the top plate allows the molecular beam

source to be inserted into the chamber. The larger aperture in the bottom plate of the chamber allows the molecular beam to escape freely from the chamber. The structure used to form the molecular beam is described below.

3.3 Molecular Beam Head and Material Handling Systems

The molecular beam is generated by injecting the gas under study into the collision chamber through a cluster of fine platinum tubes, ~ 0.2 mm inside diameter and 0.1 mm wall thickness. The arrangement of these tubes is shown to scale in Figure 3. At their outlet they form a beam of rectangular cross section with initial dimensions of 3.25×0.6 mm. The intersection with the electron beam occurs ~ 2.5 mm below the tube outlets. The inlet to the tube cluster is fed with HgBr_2 vapor and/or a permanent gas, normally He, using the arrangement shown to scale in Figure 4.

The HgBr_2 used in the present study was made by reacting high purity mercury and bromine and doubly distilling the product. It is incorporated into the apparatus in a sealed capsule holding approximately 6 grams. In this way it was possible to complete all routine operations of the system, including the acquisition of He calibration data, prior to exposing the system to HgBr_2 vapor. When required, the HgBr_2 capsule could be cracked open by depressing the bellows sealed plunger mechanism shown in Figure 4. The HgBr_2 vapor pressure is then controlled by proper adjustment of the combination of heaters and/or use of the cooling head connected to the HgBr_2 reservoir by a thick copper "bridge". The cooling head consists of a vertical metal "cold finger" situated beside the HgBr_2 reservoir within the vacuum system. The cold finger is cooled from outside the vacuum system by filling it with alcohol and inserting a commercially available* freon cooled cold finger into the alcohol. The commercial cold finger was supplied as a "customized" unit, with a 2-3/4" Varian flange. This allows the alcohol filled volume to be evacuated by a small forepump, and sealed off. In this way it has been possible to maintain a HgBr_2 sample

*Neslab Bath Cooler, Model PBC-4II

within the system for many weeks after opening the capsule. The cooling system can maintain the HgBr_2 reservoir at a temperature of -13°C indefinitely, even during operation of the electron gun filament. As shown in Figure 5, the vapor pressure above a HgBr_2 sample held at this temperature is approximately 1.4×10^{-6} torr.

The temperature profile of the regions accessible to the HgBr_2 vapor, prior to its leaving the molecular beam tube cluster, is continuously monitored by six thermocouples. By appropriate individual adjustment of the four heaters the temperature profile is always maintained such that the molecular beam tube cluster is about 50°C hotter than the HgBr_2 reservoir which is the coldest region. This ensures that there is no danger of clogging of the tube cluster, and that there is no migration of condensed phase HgBr_2 away from the reservoir.

In the course of the work reported here only two capsules of HgBr_2 have been used. The first capsule provided valuable experience in operating the system and served to define the parameter ranges for subsequent systematic data collection before its contents were exhausted. All of the HgBr_2 data reported in the next section were obtained with the second HgBr_2 capsule, which at the time of writing is still in the system and is not yet exhausted.

An essential feature of the approach taken to measure the emission cross section of HgBr_2 is that the system shall permit essentially identical measurements to be made of photon emission and positive ion production in a "known" gas. This is achieved by admitting the permanent gas to the molecular beam tube cluster through a small valve shown on the right hand side of Figure 4. This valve is "normally closed", being held in that position by the two coil springs shown in Figure 4. It is opened by depressing the bellows sealed plunger. Gas is fed to this valve through a flexible bellows, which permits motion of the valve stem. The gas enters the system through the main vacuum flange on which the whole structure is mounted (see Figure 6). The small flange shown on the right in Figure 4, and in the foreground of Figure 6, seals to the underside of the main vacuum flange. Under most circumstances the small gas valve

shown in Figure 4 is kept closed, especially when the HgBr_2 vapor pressure is raised to create a HgBr_2 molecular beam. The permanent gas of interest is usually only admitted when the HgBr_2 capsule is unbroken or when the HgBr_2 reservoir is cold ($\sim -13^\circ\text{C}$). To do this the small valve is fully opened and the gas flow is controlled upstream by a Granville-Phillips variable leak valve. Occasionally it has been necessary to operate with a mixed molecular beam containing both He and HgBr_2 . On these occasions the HgBr_2 vapor pressure was kept as low as possible within the constraints of performing the measurements. With these various precautions transport of the HgBr_2 vapor was always under good control.

The overall arrangement for controlling the permanent gas, and pumping the various parts of the system, is shown schematically in Figure 7. Valve V_1 is the small valve shown in Figure 4, whose function has already been described. Valve V_2 is a bypass valve which is open during the initial pump down phase, but thereafter is normally kept closed. Valve V_3 is the Granville-Phillips variable leak valve used to control the flow of gas to the molecular beam head. The Baratron absolute pressure gauge provides a precise, reproducible measurement of the pressure at a particular point in the gas flow line from the leak valve to the molecular beam head. Under all conditions so far explored the signals produced in the collision chamber with a permanent gas beam have been found to be strictly proportional to the pressure indicated by the Baratron gauge. The remote side of the Baratron is initially evacuated through valve V_4 , which is subsequently kept closed. The vacuum on the reference side is then maintained by continuous operation of a small Penning pump.

The permanent gas backing pressure for the variable leak valve (V_3) is controlled by valves V_5 - V_8 . Two lecture bottle size gas samples can be accommodated on the manifold, allowing rapid changeover when desired.

3.4 Photon Counting System

As indicated in Figure 1 only those photons entering the small solid angle subtended by the f/3.5 optical system can be detected. Hence, in order to provide high sensitivity and wide dynamic range it was deemed necessary to use a photon counting system. In contrast to the photons, essentially all of the ions produced in the collision chamber can be collected, and easily measured. Comparison of these two measured signals indicates that at ~ 500 nm, with a resolution of 1.8 nm (FWHM), the system counts only ~ 5 photons for every million photons produced in the collision chamber.

The optical system used for all the measurements reported here is shown to scale in Figure 8. The crossed beams interaction region is viewed through a 51 mm diameter plane sapphire window in the vacuum envelope. The 51 mm diameter plano-convex quartz lens has a focal length of 75 mm. The interaction region is focussed on the entrance slit of the 1/4 meter Jarrell Ash grating monochromator. For the quantitative emission cross section measurements we chose to use 500 μ slits, giving 1.8 nm resolution (FWHM). These were the largest that could be used and still adequately resolve the He lines of interest, particularly the 504.8 nm line from the adjacent 501.6 nm line. Under other circumstances slits as narrow as 150 μ were used, and on occasions the slits were removed completely to provide the widest possible controlled bandpass, of 30 nm FWHM. All of the present measurements were performed with the 1180 grooves/mm grating blazed at 600 nm. The combination of this grating and the RCA 8575 photomultiplier gave an overall relative quantum efficiency whose dependence on wavelength was well matched to the requirements of the present experiment.

The exit slit of the monochromator is viewed by the photomultiplier operated in a thermo-electrically cooled housing.* The thermal window of the housing consists of a plane quartz window in combination with a double convex 25 mm diam. quartz lens of focal length 25 mm. It

*Products for Research Model TE104TS-RF

serves to focus the exit slit of the monochromator on the central region of the photo-cathode of the photomultiplier. A magnetic lens* restricts the effective cathode area to a central region of approximately 15 mm diameter, and was found to reduce the dark count rate by approximately a factor of 8. A manually operated optical shutter between the monochromator and the photomultiplier provides a convenient means for keeping the photomultiplier dark whenever changes are made to the rest of the system. All the optical components outside the vacuum system are rigidly coupled together and mounted on an adjustable platform which allows the focus of the whole optical system to be moved into coincidence with the crossed beams interaction region.

The only major problem encountered with the operation of the optical detection system was that initially there was a very large background signal due to scattered light originating at the electron gun filament. The problem was solved straightforwardly by enclosing the electron gun structure in an optically baffled box (not shown in Figure 6), and restricting the field of view of the sapphire window by installation of the cone shaped optical baffle shown in Figure 8. With these modifications the background signal from the scattered filament light was reduced to negligible levels at ~ 300 nm, and to a level approximately equal to the photomultiplier dark count rate ($\sim 10 \text{ s}^{-1}$) at ~ 600 nm.

In order to choose the best operating point for the photomultiplier measurements were made of both the dark count rate and the signal count rate as functions of the voltage applied to the photomultiplier and the discriminator setting of the pulse counting electronics. The latter consisted of an Ortec 9301 preamplifier (X10) coupled directly to the anode of the photomultiplier, followed by an Amplifier-Discriminator (Ortec Model 9302) operated with a gain of ten. With this arrangement optimum signal to dark counts were achieved by applying 1500 V to the photomultiplier, cooled to -30°C , and with the discriminator set at its mid-point, corresponding to a threshold of approximately 160 mV.

The output of the pulse discriminator was coupled in parallel to a Counter/Timer (Ortec Model 9315), a ratemeter (Tennelec TC 590), and when desired to the pulse counting input of a multichannel scaler

*Products for Research Model PR411

(Technical Measurement Corporation, Model No. CAT 400C). The ratemeter was used only for visual display of the instantaneous count rate, and facilitated tuning of the system. The counter/timer was used for quantitative measurements of the optical signal under fixed conditions of the experimental parameters.

The multichannel scaler has four parallel inputs, each of which may be used for pulse counting, or analogue input with its own analogue-to-digital converter. This made it possible to simultaneously record any combination of the photon signal, the transmitted electron current signal, the positive ion current signal, and the negative ion current signal as the analyzer was swept through its 4×100 channels. Sweeping of the analyzer could be performed in synchronism with the accelerating voltage sweep of the electron gun, or with the wavelength scan of the monochromator. The latter is achieved using a commercial* digitally controlled stepping motor capable of a wide range of sweep speeds. The pulse train available from this unit, with repetition rate proportional to the wavelength sweep speed, is further divided by an interface unit before use as the "channel address advance" pulse train for the multichannel scaler. In this way the effective channel width (nm/channel) is controlled independently of the monochromator sweep speed (nm/sec).

Reproducible correlation of the wavelength sweep with the channel addresses is achieved by initially setting the lower level comparator of the Omnidrive at the desired starting wavelength, and then starting the wavelength scan at a slightly lower wavelength. The voltage level change generated by the comparator when the unit passes through the set wavelength is used to generate a trigger pulse which initiates the sweep of the multichannel scaler. Tests of the system indicate that, for a fixed setting of the lower level comparator, successive sweeps are reproduced to better than one channel width of the multichannel scaler. The starting wavelength cannot, however, be reset to better than a few Angstroms.

*Jarrell-Ash Omnidrive, Model 82-462

3.5 Data Analysis

The underlying principle of the present experiment is that measurements in a known gas (He) are used to calibrate the system such that in an unknown gas we are able to determine the ratio of the emission cross section to the ionization cross section. An additional minor complication in the present case is that the calibration is performed with line emission, while the "unknown" emission is in the form of a continuum. In the following analysis it is convenient to characterize quantities measured in the calibrating gas by the subscript "l", while those relevant to the "unknown" gas have the subscript "c". The various symbols used in the analysis are listed in Table 1 together with their definitions.

In the line emitting calibrating gas it follows from the definitions that

$$eN_l(\lambda_l, \epsilon_l) = E(\lambda_l) I_{eN_l L O_l}(\lambda_l, \epsilon_l) \quad (3)$$

$$I_l^+(\epsilon_{il}) = E_l^+(\epsilon_{il}) I_{eN_l L O_{il}}(\epsilon_{il}) \quad (4)$$

We may write the ratio of Eqs. (3) and (4) in the form

$$\frac{I_l^+(\epsilon_{il})}{eN_l(\lambda_l, \epsilon_l)} \cdot \frac{E(\lambda_l)}{E_l^+(\epsilon_{il})} \cdot \frac{\sigma_l(\lambda_l, \epsilon_l)}{\sigma_{il}(\epsilon_{il})} = 1 \quad (5)$$

Similarly, for the continuum emitting gas we write

$$eN_c(\lambda_o, \epsilon_c) = I_{eN_c L} \int E(\lambda) \sigma_c(\lambda, \epsilon_c) F_s(\lambda - \lambda_o) d\lambda \quad (6)$$

and

$$I_c^+(\epsilon_{ic}) = E_c^+(\epsilon_{ic}) I_{eN_c L O_{ic}}(\epsilon_{ic}) \quad (7)$$

With the assumption that $E(\lambda)$ and $\sigma_c(\lambda, \epsilon_c)$ are essentially constant over the width W_s of the slit function $F_s(\lambda - \lambda_o)$ we may approximate Eq. (6) by

$$e \dot{N}_c(\lambda_o, \epsilon_c) = I_e N_c L E(\lambda_o) \sigma_c(\lambda_o, \epsilon_c) W_s \quad (8)$$

where
$$W_s = \int F_s(\lambda - \lambda_o) d\lambda \quad (9)$$

is the effective width of the slit function. For a triangular slit function W_s is simply the full width at half maximum (FWHM).

The ratio of Eqs. (7) and (8) gives

$$\frac{\sigma_c(\lambda_o, \epsilon_c)}{\sigma_{ic}(\epsilon_{ic})} = \frac{e}{W_s} \cdot \frac{E_c^+(\epsilon_{ic})}{E(\lambda_o)} \cdot \frac{\dot{N}_c(\lambda_o, \epsilon_c)}{I_c^+(\epsilon_{ic})} \quad (10)$$

Multiplying Eq. (10) by Eq. (5) gives

$$\frac{\sigma_c(\lambda_o, \epsilon_c)}{\sigma_{ic}(\epsilon_{ic})} = \frac{1}{W_s} \cdot \frac{R^+}{R(\lambda_o)} \cdot \frac{\sigma_\ell(\lambda_\ell, \epsilon_\ell)}{\sigma_{i\ell}(\epsilon_{i\ell})} \cdot \frac{I_\ell^+(\epsilon_{i\ell})}{\dot{N}_\ell(\lambda_\ell, \epsilon_\ell)} \cdot \frac{\dot{N}_c(\lambda_o, \epsilon_c)}{I_c^+(\epsilon_{ic})} \quad (11)$$

where
$$R^+ = \frac{E_c^+(\epsilon_{ic})}{E^+(\epsilon_{i\ell})} \quad (12)$$

is the relative ion collection efficiency

and
$$R(\lambda_o) = \frac{E(\lambda_o)}{E(\lambda_\ell)} \quad (13)$$

is the relative quantum efficiency (RQE) at wavelength λ_o compared to the line emission wavelength.

Integrating Eq. (11) over wavelength λ_o gives the ratio of total continuum emission cross section

$$\sigma_c(\epsilon_c) = \int \sigma_c(\lambda_o, \epsilon_c) d\lambda_o \quad (14)$$

to the ionization cross section

$$\frac{\sigma_c(\epsilon_c)}{\sigma_{ic}(\epsilon_{ic})} = \frac{R^+}{W_s} \cdot \frac{\sigma_\ell(\lambda_\ell, \epsilon_\ell) I_\ell^+(\epsilon_{ic})}{\sigma_{ic}(\epsilon_{ic}) \dot{N}_\ell(\lambda_\ell, \epsilon_\ell)} \left[\frac{\dot{N}_c(\lambda_o, \epsilon_c) d\lambda_o}{R(\lambda_o) I_c^+(\epsilon_{ic})} \right] \quad (15)$$

The positive ion current measured in the continuum case is retained within the integral in recognition of the possible variation of neutral beam density during the measurement of $\dot{N}_c(\lambda_o, \epsilon_c)$ over the necessary wavelength region. In the present experiment the wavelength dependence of $\dot{N}_c(\lambda_o, \epsilon_c)$ is measured at fixed energy ϵ_c by scanning the monochromator at constant speed S nm/sec, and storing the resulting counts in the multi-channel scaler where each channel has the corresponding width W_{ch} in nm. If the counts accumulated in channel n number $N_c(n)$, and the center wavelength of the channel is λ_n , then we may write

$$\dot{N}_c(\lambda_n) = \frac{S [N_c(n) - B(n)]}{W_{ch}} \quad (16)$$

for substitution into Eq. (11).

Similarly, in Eq. (15) we replace the integral by the summation

$$S \sum \frac{[N_c(n) - B(n)]}{R(\lambda_n) I_c^+(\epsilon_{ic})} \quad (17)$$

where we have corrected the signal for background. Hence, for final working formulae we arrive at

$$\frac{\sigma_c(\lambda_n, \epsilon_c)}{\sigma_{ic}(\epsilon_{ic})} = \frac{A}{W_{ch}} \left[\frac{N_c(n) - B(n)}{R(\lambda_n) I_c^+(\epsilon_{ic}, n)} \right] \quad (18)$$

$$\frac{\sigma_c(\epsilon_c)}{\sigma_{ic}(\epsilon_{ic})} = A \int \left[\frac{N_c(n) - B(n)}{R(\lambda_n) I_c^+(\epsilon_{ic}, n)} \right] \quad (19)$$

where

$$A = \left[\frac{\sigma_\ell(\lambda_\ell, \epsilon_\ell)}{\sigma_{i\ell}(\epsilon_{i\ell})} \right] \left[\frac{S}{W_s} \right] \left[R^+ \right] \left[\frac{I_\ell^+(\epsilon_{i\ell})}{N_\ell(\lambda_\ell, \epsilon_\ell)} \right] \quad (20)$$

For each wavelength scan of the continuum A is a constant of the instrument. In Eq. (20) the quantities in the first bracket are taken from the literature, those in the second are controlled experimental parameters, that in the third (see Eq. 11) is an experimental parameter depending on the operating conditions, and must be measured, and those in the final bracket are directly measured quantities.

The effective width, W_s , of the normalized slit function is determined by the dispersion of the grating and the geometric width of the slits of the monochromator. It can easily be measured by scanning a line whose true width is much smaller than W_s using a channel width $W_{ch} \ll W_s$. Under these conditions

$$W_s = \frac{W_{ch} \sum [N_\ell(n) - B(n)]}{N_\ell(n_\ell) - B(n_\ell)} \quad (21)$$

where n_ℓ is the channel number corresponding to λ_ℓ , and the summation encompasses an appropriate number of channels on each side of n_ℓ .

4. RESULTS

4.1 Wavelength Dependence of the Quantum Detection Efficiency

Measurement of the unknown continuum emission cross section involves the use of Eqs. (18) and (19) derived in the previous section. These require a knowledge of the relative quantum efficiency $R(\lambda_o)$, defined by Eq. (13)

$$R(\lambda_o) = \frac{E(\lambda_o)}{E(\lambda_\ell)} \quad (13)$$

We recall that λ_ℓ is the wavelength of the line radiation used as a known reference. In the present work we have used the 504.8 nm (4^1S-2^1P) radiation from He as our primary reference, and thus adopt $\lambda_\ell = 504.8$ nm in using Eq. (13).

In the present experiment the $HgBr^*(B)$ state molecules are formed under essentially collisionless conditions, since the $HgBr_2$ beam density is typically $\sim 10^{12} \text{ cm}^{-3}$. This number is computed from the measured ion signal and the known ionization cross section (Wiegand & Boedeker, 1982). In this situation we expect from previous work (Wieland, 1932; Chang & Burnham, 1980; Roxlo & Mandl, 1980) that the emission spectrum will extend from approximately 510 nm to ~ 300 nm. It is therefore necessary to measure $R(\lambda_o)$ over at least this range. This necessitated the use of two standard lamps. For the shorter wavelengths a deuterium arc discharge lamp*, calibrated over the range 180 to 400 nm, was used. Scans of the output were performed over the range 250 to 400 nm. For longer wavelengths a tungsten halogen filament lamp** was used. The calibration data supplied with this lamp extends from 250 to 2500 nm.

*Optronic Laboratories, Inc. Model IV-40

**The Eppler Laboratory, Inc. Model ES-8203

For the present purpose, however, scans were performed only from 250 to 650 nm. In the region of overlap of the two lamps the resulting curves showed excellent agreement between 320 nm and 400 nm. Below 320 nm the system response to the tungsten halogen lamp was anomalously high, due to scattered light of longer wavelengths. This effect was to be expected since the tungsten halogen lamp's photon output is steadily increasing with wavelength over the range of interest, and at 650 nm is a factor of 100 greater than at 320 nm.

A non-trivial problem in performing the standard lamp measurements was that the lamps were many orders of magnitude too bright for the photon counting system. The resolution adopted was to arrange a narrow transverse slit at the focus of optical system, and to illuminate this slit from a distance of approximately ten feet. The lamps were placed in a light-tight enclosure containing a small hole to provide line of sight between the lamp and the optical system. The system viewed the lamp through a long tube, a few inches in diameter, which served to prevent scattered light from other parts of the room from entering the system.

The procedure adopted for each scan was as follows. Having set the starting wavelength of the automatic scan of the monochromator, a scan was first made of the spectrum emitted by a Hg discharge lamp.* This served to calibrate the wavelength scale for the subsequent scan of one or other standard lamp. Prior to scanning the standard lamp, spot measurements were made of the photon count rate at typically three specified wavelength settings of the monochromator. These readings were repeated after the wavelength scan of the lamp, as was the scan of the Hg lamp. In this way the constancy of lamp output during the scan was checked, and the wavelength scale repeatability was confirmed. In all cases the lamp output was found to be steady to within 1 or 2% over the period of a scan. Each scan of a lamp was corrected for background by repeating the scan with the light blocked off at the output of the lamp enclosure, and with the MCS operated in the "subtract" mode. The resulting calibration curve for the optical system is shown in Figure 9. The

*Ultra-Violet Products, Inc. Penray lamp

curve is a composite of two scans of the D₂ lamp, and three scans of the tungsten-halogen lamp. Note that the value of the relative quantum efficiency has been set equal to unity at the chosen reference wavelength of 504.8 nm, corresponding to the primary helium calibration line.

4.2 Helium Line Calibration Data

The objective of these particular measurements was to evaluate the quantity

$$\left[\frac{\sigma_{\ell}(\lambda_{\ell}, \epsilon_{\ell})}{\sigma_{i\ell}(\epsilon_{i\ell})} \cdot \frac{I_{\ell}^{+}(\epsilon_{i\ell})}{N_{\ell}(\lambda_{\ell}, \epsilon_{\ell})} \right]$$

appearing in the "instrument constant" A defined by Eq. (20). Because of its proximity to the peak of the HgBr(B-X) fluorescence the He 504.8 nm (4¹S-2¹P) line was chosen as the reference calibration line, with the He 443.8 nm (5¹S-2¹P) and He 416.9 nm (6¹S-2¹P) lines providing additional calibration points. All three lines were included in the benchmark cross section measurements of Van Zyl et al. (1980). The relevant quantities from this publication, and that of Rapp & Englander-Golden (1965) are listed in Table 2.

Exploratory scans of the helium spectrum indicated that well resolved measurements of the line radiation at 504.8 nm would necessitate the use of the 500 μ slits, due to the adjacent radiation at 501.6 nm. The observed line shapes of isolated lines were found to be essentially triangular, with slightly flattened peaks, and FWHM of 1.7 ± 0.1 nm. More importantly, the "effective line width" W_s , defined by Eq. (9), was evaluated using Eq. (21) for a number of lines, including the calibration lines, giving $W_s = 1.80 \pm 0.05$ nm.

He calibration measurements were performed before and after the HgBr₂ measurements described in a later subsection. The reproducibility over this period was typically better than 5% and in only a few cases exceeded 10%. Generally speaking, measurements were taken at three

different pressures. It was established in a series of exploratory measurements that the ion currents and the photon count rates corrected for background were directly proportional to both the pressure indicated by the Baratron gauge, and the measured transmitted electron current. Most of the He calibration data was taken with an electron current of 5×10^{-6} amps - a value well within the explored range.

An example of a set of measurements at $\lambda_\ell = 504.8$ nm and at $\lambda_\ell = 443.8$ nm is shown in Table 3. Note that the present $\epsilon = 35$ eV measurements cannot be used in the evaluation of the quantity $[(\sigma_\ell I_\ell^+)/(\sigma_{i\ell} \dot{N}_\ell)]$, shown in the final column, because the line emission cross section at this energy is not given by Van Zyl et al. The quantity shown in the final column of Table 3 for this energy is actually the mean of the values determined from the measurements at the other three energies. For this reason it is distinguished by the square brackets. It has been used to "back out" the corresponding values of $\sigma_\ell/\sigma_{i\ell}$ shown in the third column of Table 3, which in turn have been used to derive the values of $\sigma_\ell(\lambda_\ell, 35)$ shown in Table 2.

In general we expect

$$\left[\frac{\sigma_\ell(\lambda_\ell) I_\ell^+}{\sigma_{i\ell} \dot{N}(\lambda_\ell)} \right] R(\lambda_\ell) = \frac{\sigma_\ell(504.8) I_\ell^+}{\sigma_{i\ell} \dot{N}_\ell(504.8)} \quad (22)$$

where $R(\lambda_\ell)$ is the relative quantum efficiency plotted in Figure 9. Hence, the measurements performed at 443.8 nm and at 416.9 nm can be converted to equivalent calibration data at 504.8 nm., represented by the right hand side of Eq. (22). Based on data at all three wavelengths an overall mean value of $(3.37 \pm 0.20) \times 10^{-14}$ is obtained for the right hand side of Eq. (22). This value was arrived at in two ways. It represents the mean value from all the relevant measurements. The same number was obtained after making an attempt to select the "best" data on the basis of general consistency, signal to background and reproducibility.

We note from Eq. (5) that this number, when divided by the ion collection efficiency and the fundamental electron charge, gives the reciprocal of the overall photon counting efficiency, $E(\gamma)_c$. Using the value of 0.95 for E_c^+ , the ion collection efficiency in He determined from saturation curve measurements described below, we arrive at a value of

$$E(504.8 \text{ nm}) = 4.5 \times 10^{-6} \quad (23)$$

4.3 Relative Ion Collection Efficiencies

In any particular case the ion collection efficiency (E^+ in Eqs. (4) and (7) depends on the strength of the ion collection field applied between the ion attractor and ion repeller electrodes, shown in Figures 1 and 2, and on the initial kinetic energy of the ions when formed. For parent ions this energy is simply the initial thermal energy of the neutral precursor, and such ions are relatively easy to collect. In He this is the only possibility. An example ion saturation curve is shown in Figure 10. With other conditions fixed the collected ion current quickly "saturates" as the extraction voltage V_{ext} is raised. Based on data of this type we chose $V_{\text{ext}} = 6\text{V}$ as a suitable condition for performing the various other measurements. It is clear from the figure that at this value of extraction field a large fraction of the ions is collected. An estimate of the exact fraction can be conveniently made by plotting the data as a function of $(V_{\text{ext}})^{-1}$, and extrapolating to infinite extraction field. This procedure is illustrated in Figure 10. For helium it gives a value of $E_c^+(\text{He}) = 0.95 \pm 0.02$.

In HgBr_2 the situation is more complicated because of the relatively large fraction of fragment ions formed at electron energies above ~ 20 eV. For purposes of the present experiment it was convenient to routinely measure the reference ion current signal $I_c^+(e_{\text{ic}})$ in HgBr_2 at an energy of $e_{\text{ic}} = 50$ eV. At this energy, according to the data of Wiegand and Boedeker (1982), approximately 68% of the ions are HgBr_2^+ , the remainder being primarily HgBr^+ and Br^+ fragment ions. Ion saturation curves of the type presented in Figure 10 for He were also measured in

HgBr₂ at energies of 15 eV and 50 eV. These curves indicated that at 15 eV it was relatively easy to collect most of the ions, a value of $E_c^+(15) = 0.95$ being obtained for $V_{ext} = 6V$. At 50 eV, however, it was clearly more difficult to collect the ions, and a value of $E_c^+(50) = 0.77 \pm 0.03$ was obtained for $V_{ext} = 6V$. Hence the value of

$$R^+ = \frac{E_c^+(\text{HgBr}, 50 \text{ eV})}{E_c^+(\text{He})} = \frac{0.77 \pm 0.03}{0.95 \pm 0.02} = 0.81 \pm .05 \quad (24)$$

was obtained for use in evaluating the "instrument constant" A given by Eq. (20).

To recapitulate the measurements described so far, we have determined that for the chosen standard operating conditions

$$\frac{\sigma_\ell(504.8) I_\ell^+(\epsilon_{i\ell})}{\sigma_{i\ell}(\epsilon_{i\ell}) \dot{N}_\ell(504.8)} = (3.37 \pm 0.20) \times 10^{-14}$$

$$W_s = 1.80 \pm 0.05 \text{ nm}$$

and $R^+ = 0.81 \pm 0.05$

It follows from Eq. (20) that

$$A = S \times (1.52 \pm .22) \times 10^{-14} \text{ Amps/photon count} \quad (25)$$

where S = monochromator scan speed in nm/S.

4.4 Measurements in HgBr₂

Exploratory measurements in HgBr₂ soon established that the emission cross section is sufficiently large that systematic measurements could be conducted at relatively low beam densities - typically 10^{12} cm^{-3} , and that the emission extended from $\sim 510 \text{ nm}$ to approximately 300 nm once the electron energy was raised a few volts above threshold.

Basically two types of measurements were performed, both involving scans with the multichannel scaler (MCS). The first type of scan served to record the dependence of the various signals on electron energy. As explained in Section 3.4, any combination of the transmitted electron current, the collected positive ion current, the collected negative ion current, and the photon counts could be accumulated in the four sections of the 4×100 channels of the MCS. In most instances the positive ion signal and the photon signal were accumulated, but the negative ion signal was also recorded during many of the scans. An example of the raw data from such a scan is shown in Figure 11. Note that the data is recorded as a function of the electron accelerating voltage, but is plotted here as a function of electron mean energy (i.e., corrected for contact potentials) by setting the scale such that the threshold for the appearance of positive ions occurs at the correct value of 10.6 eV . This value of the ionization potential is taken from the work of Eland (1970), and was confirmed in the present experiment by measuring the positive ion appearance curve for an appropriate mixture of HgBr₂ and He, such that both the initial threshold at 10.6 eV , and the break at 24.5 eV could be precisely located. The curves so measured indicated that these two points are indeed displaced by 13.9 volts on the electron accelerating voltage scale. A large number of scans of this general type were taken for purposes of measuring at frequent time intervals the correction to be applied to the electron accelerating voltage scale in order to derive the corrected electron energy. The consensus of these curves was that the threshold for the B-X fluorescence signal is at $6.0 \pm 0.1 \text{ eV}$, and that the cross section rises rapidly from threshold, "saturating" a few eV above threshold.

The structure in the photon curve visible in Figure 11 is very reproducible, and this type of structure appears whenever the optical system bandpass wavelength is set in the region of the peak emission at ~ 503 nm. Data of this type gives directly the electron energy dependence of a wavelength resolved cross section - the particular wavelength, or wavelength range involved depending on the setting of the monochromator, and the slit widths used. The calibration of such curves to give the cross section in cm^2/nm could be performed using modified forms of Eqs. (18) and (20), where S in Eq. (20) becomes the MCS scan speed in channels/sec., and W_{ch} is eliminated from Eq. (18). In the present work, however, it was convenient to make all such calibrations via the data taken in a second mode, where the electron energy was fixed and the photon counts stored in the MCS as a function of wavelength.

Two examples of the raw data, obtained by scanning the monochromator wavelength synchronously with the MCS as explained in Section 3.4, are shown in Figure 12. The conditions for these scans are indicated in the caption. In these cases, and many others, two wavelength scans, (280-440 nm) and (390-550 nm), were used at each energy to efficiently cover the whole range of interest. The region of overlap, 390-440 nm, gave a valuable consistency check between the two runs. The two sets of data shown in Figure 12 serve to illustrate the changing nature of the emission spectrum as the electron energy is raised from the threshold value (6.0 eV). At low energies the extent of the continuum to shorter wavelengths is limited by the available energy and there is no evidence of individual atomic mercury lines. As the energy is raised the shape of the B-X continuum is quickly established, and changes little for electron energies above ~ 9 eV. Also, at energies above ~ 8 eV, there is increasing evidence of the C-X emission band in the region of 300 nm. At somewhat higher energies, above ~ 10 eV, there is increasing evidence of atomic mercury lines. They are clearly visible in the 16.1 eV spectrum shown in Figure 12, and in general provided a convenient means of wavelength calibration.

A few spectra of the type shown in Figure 12 were taken with improved spectral resolution (150 μ slits), and multiple scans in the 500 nm region to improve the signal-to-random noise ratio. From such scans it was evident that, near threshold, the spectrum is highly structured, allowing individual $v''-v'$ transitions to be assigned. As the electron energy was raised above threshold, however, this structure quickly became unresolvable, presumably due to additional higher $v''-v'$ transitions entering the spectrum.

Data of the type displayed in Figure 12 was taken at various electron energies spanning the range from threshold to 35 eV. The numerical data were printed systematically for each scan, and in all cases a record was made of the reference ion current signal, at 50 eV, both immediately before and immediately following the scan. Typically, these differed by less than 10%, and a linear interpolation procedure was adopted to derive the reference ion current appropriate to each channel of data. The corrected data for each channel, namely

$$\frac{N_c(n) - B(n)}{R(\lambda_n) I_c^+(50, n)} \quad (26)$$

was computed for each channel. Use of equations (18) and (19), the known values of A given by Eq. (25), and the set parameters S (scan speed) and W_{ch} (MCS channel width), allowed both the wavelength resolved cross section $\sigma_c(\lambda_n, E_c)$ and the total band emission cross section $\sigma_c(E_c)$ to be derived from the data. In the latter case it was necessary at the higher electron energies to subtract from the integrated corrected counts the contributions from Hg line emissions, and the overlapping contribution at short wavelengths from the C-X fluorescence. The latter correction was difficult to make precisely, and some uncertainty is present in the resulting values of $\sigma_c(E_c)$ at energies above 8 eV.

As is evident from Eq. (18) and (19), the present experiment serves to determine the emission cross section relative to the $HgBr_2$ total

ionization cross section at the reference energy (50 eV). We employ here the value of $1.85 \times 10^{-15} \text{ cm}^2$ measured by Wiegand and Boedeker, and note that any error in this cross section, or in the emission cross sections of Van Zyl et al., will automatically appear as a scaling error in the values of $\sigma_c(\lambda, \epsilon_c)$ and $\sigma_c(\epsilon_c)$ presented here.

Examples of the wavelength resolved absolute emission cross sections derived by the above procedure are shown in Figure 13. The curves shown are smoothed versions of plots of corrected data, all of which showed scatter of the data points similar to that seen in Figure 12. In all probability some real structure in the cross sections has been removed. An interesting feature of the curves may be noted in this figure. The peak cross section, in the region of $\lambda = 503 \text{ nm}$ tends to oscillate with increasing electron energy. This same effect was noted in relation to the data presented in Figure 11. So far as can be determined these oscillations are not present in the total emission cross section, $\sigma_c(\epsilon)$ derived by numerical summation using Eq. (19). The results obtained in this way are shown in Figure 14 by the open circles. Where two connected circles are shown they indicate the results obtained by two extreme approaches, admittedly somewhat subjective, being applied to the problem of separating the B-X and C-X fluorescence in the region of overlap.

For comparison we also show in Figure 14 wavelength resolved data, represented by solid points. The low energy data, between 1 and 21 eV was taken with the broadest possible controlled bandpass of the monochromator, obtained by removing the slits completely. Measurements in He of the dominant line radiation at 389.3 nm indicated that, with this arrangement, the effective slit function has a FWHM of 30 nm. The low energy solid points in Figure 14 were taken with this bandpass centered at 495 nm. Inspection of Figures 12 and 13 shows that under these conditions most of the prominent peak at $\sim 500 \text{ nm}$ is passed by the instruments. This gave a sufficiently large photon signal for the effective electron energy resolution to be improved by operation of the electron gun in the Retarding Potential Difference (RPD) mode (Chantry, 1969), giving an energy resolution in this case of $\sim 0.2 \text{ eV}$.

The higher energy solid points were obtained in a separate scan covering the energy range 0-200 eV with much coarser energy resolution, and a narrower bandpass centered at ~ 503 nm. This set of data was merged with the lower energy set in the region of overlap, and both were scaled to agree with the peak values of the wavelength resolved emission cross section from data such as that displayed in Figure 13. The higher energy region of the total emission cross section, shown by the broken curve in Figure 14, was estimated by adopting the same shape as that given by the high energy solid points. This procedure was based on the observation that the shape of the continuum emission spectrum was essentially independent of electron energy above approximately 20 eV.

Throughout the present work no evidence was found for B-X emission at electron energies below the threshold of 6.0 ± 0.1 eV measured for reaction 1. In particular, there was no evidence for the occurrence of reaction (2) in the region of 3-5 eV where Br^- production has been established to occur, by Wiegand and Boedeker (1982). An upper limit may be placed on the magnitude of the cross section by plotting the low energy (1-21 eV), wide bandpass (480-510 nm), RPD data on semi-logarithmic paper, as displayed in Figure 15. From this we may conclude that in the 3-5 eV region the B-X emission cross section is at least three orders of magnitude smaller than the plateau value above ~ 10 eV. Hence a conservative statement would be that the cross section for reaction (2) in this region of energy is less than 10^{-18} cm^2 .

5. DISCUSSION

The total $\text{HgBr}^*(B^2\Sigma_{1/2}) \rightarrow X^2\Sigma_{1/2}$ continuum emission cross section determined in the present study is significantly larger, and has a lower threshold, than the cross sections inferred by either Hsia et al. (1981), or by Nighan and Brown (1982). A direct comparison of these three cross sections is shown in Figure 16. The impact of this on the overall laser modelling has not yet been fully established, but at a minimum it will require adjustments to be made in the present estimates of the other inelastic energy loss processes in HgBr_2 , at present assumed to occur at 5 eV and 7.9 eV. Preliminary estimates of these changes by Kline et al. (1982) suggest that the magnitude of the cross section assumed to have a 5 eV threshold must be increased substantially.

The only other experimental measurement of this cross section is that reported by Allison and Zare (1978). Some of the problems associated with that measurement were discussed in Section 2. We could in principle compare their measurement of the "cross section for the most intense transition" at 501.8 nm, at, say 200 eV where they report a value of 10^{-19} cm^2 , with our own measurements. However, these authors did not report the effective slit width of their optical system. We infer from our own measurements of $\sigma_c(\lambda, \epsilon)$ in this region that their effective slit width must have been approximately 0.05 nm.

ACKNOWLEDGEMENTS

The authors are indebted to a number of their colleagues for their assistance and interest during this project. The experiment would not have been possible without the expert technical work of W. M. Uhlig, W. F. Toth and C. S. Spontak in constructing the apparatus. W. D. Partlow and J. T. Veligdan generously loaned us important optical components, and C. Hirayama provided the HgBr_2 capsules. L. E. Kline and C. S. Liu were participants in a number of useful discussions. The authors are also appreciative of the encouragement, interest and understanding of M. B. White of the Office of Naval Research, Boston.

This report was typed by Toni McElhaney.

REFERENCES

- Allison, J. and Zare, R. N. (1978) Chem. Phys. 35, 263-7.
- Chang, R.S.F. and Burnham, R. (1980) Appl. Phys. Lett. 36, 397-400.
- Chantry, P. J. (1969) Rev. Sci. Instr. 40, 884-9.
- Degani, J., Rokni, M. and Yatsiv, S. (1981) J. Chem. Phys. 75, 164-170.
- Eland, J.H.D. (1970) Int. J. Mass Spectrom. Ion Phys. 4, 37-49.
- Fox, R. E., Hickam, W. M., Grove, D. J. and Kjeldaas, T. (Jr.) (1955) Rev. Sci. Instr. 26, 1101-7.
- Hsia, J. C., McGeoch, M. W. and Klimek, D. E. (1981) Final Report, Contract N00123-80-C-1135 October 1981. See also McGeoch, M. W., Hsia, J. C. and Klimek, D. E. "HgBr(B) Formation by Electron Impact in HgBr₂/Noble Gas Discharges" - submitted to J. Chem. Phys.
- Kiser, R. W., Dillard, J. G. and Dugger, D. L. (1968) Advan. Chem. Ser. 72, 153.
- Kline, L. E., Chen, C. L., Chantry, P. J. and Denes, L. J. (1982). Abstract submitted to Gaseous Electronics Conference, Dallas, Oct. 1982.
- Nighan, W. L. (1980) Appl. Phys. Lett. 36, 173-175.
- Nighan, W. L. and Brown, R. T. (1982) UTRC Report No. R82-925096-1. Final Report to Contract No. N00014-80-C-0247.
- Nighan, W. L., Hinchey, J. J. and Wiegand, W. J. (1982). UTRC Report No. R82-925545-1. Final Report to Contract N00014-81-C-0253.
- Nygaard, K. J. (1981) Annual Report to Contract No. N00014-77-C-0100.
- Parks, J. H. (1977) Appl. Phys. Letts. 31, 297-300.

- Rapp, D. and Englander-Golden, P. (1965) J. Chem. Phys. 43, 1464-79.
- Roxlo, R. and Mandl, A. (1980) J. Chem. Phys. 72, 541-543.
- Schimitschek, E. J., Celto, J. E. and Trias, J. A. (1977) Appl. Phys. Lett. 31, 608-610.
- Spence, D. and Dillon, M. A. (1981) - unpublished data. See Argonne National Lab. Annual Report ANL-80-115 Pt. I 57-62.
- Van Zyl, B., Dunn, G. H., Chamberlain, G., and Heddle, D.W.O. (1980) Phys. Rev. A 22, 1916-1929.
- Wiegand, W. J. and Boedeker, L. R. (1982) Appl. Phys. Lett. 40, 225-227.
- Wieland, K. (1932) Z. Phys. 77, 157-165.

Table 1: Definition of Symbols

<u>Symbol</u>	<u>Units</u>	<u>Definition</u>
$B(n)$	counts	Background counts for channel n
e	coulombs	Electronic charge
$E(\lambda)$		Overall counting efficiency for photons of wavelength λ
$E_{\ell}^{+}(\epsilon_{i\ell})$		Positive ion collection efficiency for line emitting gas at electron energy $\epsilon_{i\ell}$
$E_c^{+}(\epsilon_{ic})$		Ditto for continuum emitting gas
$F_s(\lambda - \lambda_0)$		Normalized slit function of monochromator $F_s(0) = 1$
I_e	amps	Transmitted electron current
$I_{\ell}^{+}(\epsilon_{i\ell})$	amps	Measured ion current in the line emitting gas, at electron energy $\epsilon_{i\ell}$
$I_c^{+}(\epsilon_{ic})$	amps	Ditto for continuum emitting gas
L	cm	Length of interaction region of crossed beams
N	cm^{-3}	Average neutral density in interaction region
$N_c(n)$	counts	Photon counts accumulated in channel n of MCS
$\dot{N}_{\ell}(\lambda_{\ell}, \epsilon_{i\ell})$	counts-s^{-1}	Photon count rate when tuned to line emission at λ_{ℓ} at electron energy $\epsilon_{i\ell}$
$\dot{N}_c(\lambda_0, \epsilon_{ic})$	counts-s^{-1}	Photon count rate from continuum measured at monochromator setting λ_0 at electron energy ϵ_{ic}
R^{+}		Relative ion collection efficiency ($= E_c^{+}/E_{\ell}^{+}$)
$R(\lambda)$		Relative quantum efficiency [$= E(\lambda)/E(\lambda_{\ell})$]

Table 1: Definition of Symbols (Cont'd.)

<u>Symbol</u>	<u>Units</u>	<u>Definition</u>
S	nm-s^{-1}	Monochromator sweep speed
W_s	nm	Effective width of normalized slit function
W_{ch}	nm/ch.	Effective channel width of MCS for wavelength scans
ϵ	eV	Electron energy
λ	nm	Wavelength
λ_l	nm	Wavelength of line emission
λ_o	nm	Wavelength setting of monochromator
$\sigma_l(\lambda_l, \epsilon_l)$	cm^2	Total emission cross section for line centered at λ_l , for electrons of energy ϵ_l
$\sigma_{il}(\epsilon_{il})$	cm^2	Total ionization cross section for line emitting gas at electron energy ϵ_{il}
$\sigma_c(\lambda, \epsilon_c)$	cm^2/nm	Continuum emission cross section at wavelength λ for electrons of energy ϵ_c
$\sigma_c(\epsilon_c)$	cm^2	Total continuum emission cross section at electron energy ϵ_c
$\sigma_{ic}(\epsilon_{ic})$	cm^2	Total ionization cross section for continuum emitting gas at electron energy ϵ_{ic}

Table 2: Helium Ionization ($\sigma_{i\ell}$) and Line Emission (σ_ℓ) Cross Section

Reference Data from Literature

ϵ_ℓ eV	b		
	a	$\sigma_{i\ell}(\epsilon_\ell)$ (-16) cm^2	$\sigma_\ell(443.8, \epsilon_\ell)$ (-20) cm^2
35	0.125	$\sigma_{i\ell}(504.8, \epsilon_\ell)$ (-20) cm^2	$\sigma_\ell(416.9, \epsilon_\ell)$ (-20) cm^2
50	0.243	(9.45) c	(1.66) c
100	0.366	8.08	1.46
150	0.369	5.61	0.97
		4.60 d	0.77 d

a) Rapp & Englander-Golden (1965)

b) Van Zyl et al. (1980)

c) Derived from present measurements

d) Interpolated from 100 eV and 500 eV data points

Table 3: Examples of He Line Radiation Calibration Measurements

λ nm	E eV	$\frac{I_{\lambda}(\lambda_{\text{He}})}{\sigma_{\text{He}}(\epsilon_{\text{He}})}$	P. (Bar.) Torr	$I_{\lambda}(\lambda_{\text{He}})$ (-9) A	$\dot{N}_{\text{He}}(\lambda_{\text{He}})$ -B _{He}	$\frac{I_{\text{He}}}{\dot{N}_{\text{He}}}$	$\frac{\sigma_{\text{He}} I_{\text{He}}}{\sigma_{\text{He}} \dot{N}_{\text{He}}}$
504.8 R(1)	35	[7.56(-3)]	0.626 0.893	2.38 3.38	519 777	0.459 (-11) 0.435 (-11)	[3.38(-14)]
	50	3.33(-3)	0.622 0.890	4.50 6.70	455 677	0.99 (-11) 0.99 (-11)	3.30(-14)
	100	1.53(-3)	0.618 0.882	7.65 11.3	342 513	2.24 (-11) 2.20 (-11)	3.40(-14)
	150	1.25(-3)	0.615 0.885	8.40 12.40	305 451	2.75 (-11) 2.75 (-11)	3.44(-14)
443.8 R(1)	35	[3.08(-3)]	0.605 0.914	2.28 3.40	225 355	1.01 (-11) 0.96 (-11)	[3.05(-14)]
	50	1.27(-3)	0.603 0.911	4.35 6.90	197 316	2.21 (-11) 2.18 (-11)	2.79(-14)
	100	6.28(-4)	0.600 0.907	7.3 11.6	147 231	4.97 (-11) 5.02 (-11)	3.14(-14)
	150	5.15(-4)	0.597 0.904	8.05 12.8	129 205	6.24 (-11) 6.24 (-11)	3.21(-14)

FIGURE CAPTIONS

- Fig. 1 Schematic of crossed beam system
- Fig. 2 Horizontal section of collision chamber
- Fig. 3 Molecular beam head
- Fig. 4 HgBr₂ reservoir, molecular beam head and valve control system for permanent and reference gases
- Fig. 5 HgBr₂ vapor pressure curve as a function of inverse temperature
- Fig. 6 Photograph of apparatus
- Fig. 7 Schematic diagram of gas handling and pumping system
- Fig. 8 Schematic diagram of optical system. L1 and L2 are quartz lenses, S1 and S2 are entrance and exit slits of the Jarrell-Ash 0.25 meter Ebert monochromator. Two light baffles (out of five) shown are designed to cut down scattered light from heated filament entering the optical system.
- Fig. 9 Relative photon counting efficiency $R(\lambda_0)$ of the optical system as a function of wavelength determined with deuterium discharge and tungsten halogen standard lamps.
- Fig. 10 Helium positive ion saturation current I^+ curve as a function of extraction voltage V_{ext} (solid points) applied to the pair "attractor" and "repeller" electrodes. The open circles are plots of I^+ versus V_{ext}^{-1} .
- Fig. 11 HgBr(B-X) band fluorescence raw data at 502 nm as a function of electron energy ϵ . The slit width of the Jarrell-Ash 0.25 meter spectrometer is wide open. In this figure we also show the positive ion current I^+ and the negative ion current I^- collected by the "repeller" and "attractor" electrodes, respectively. Except shapes and positions, there is no significance of the relative magnitude of these three sets of data.
- Fig. 12 Photon counts of HgBr(B-X) fluorescence as a function of wavelength λ at electron energy $\epsilon = 6.3$ and 16.1 eV. The mercury lines at 313.1, 366.3, 435.8 and 546.1 nm are used for wavelength calibrations. The HgBr(C-X) fluorescence below Hg 313.1 nm is clearly observable at $\epsilon = 16.1$ eV.

- Fig. 13 Wavelength resolved emission cross section $\sigma_c(\lambda, \epsilon_c)$ of $\text{HgBr}^*(\text{B-X})$ for electron energies $\epsilon_c = 6.3, 7.1, 8.1$ and 9.1 eV.
- Fig. 14 A linear plot of total emission cross section $\sigma_c(\epsilon)$ of $\text{HgBr}^*(\text{B-X})$ versus electron energy ϵ . In this figure we also present a wavelength resolved emission cross section as a function of electron energy, the pass band of the optical system is $480\text{--}510$ nm (FWHM) centered at 495 nm.
- Fig. 15 A semi-log plot of wavelength resolved emission cross section versus electron energy. The Jarrell-Ash 0.25 meter Ebert spectrometer was operated without slits and the grating was set at 495 nm. The measured instrument function has a full width at half maximum of 30 nm.
- Fig. 16 Comparison of McGeoch's (AVCO) and Nighan's (UTRC) inferred $\text{HgBr}^*(\text{B-X})$ emission cross sections to the present measured one .

Dwg. 7739A23

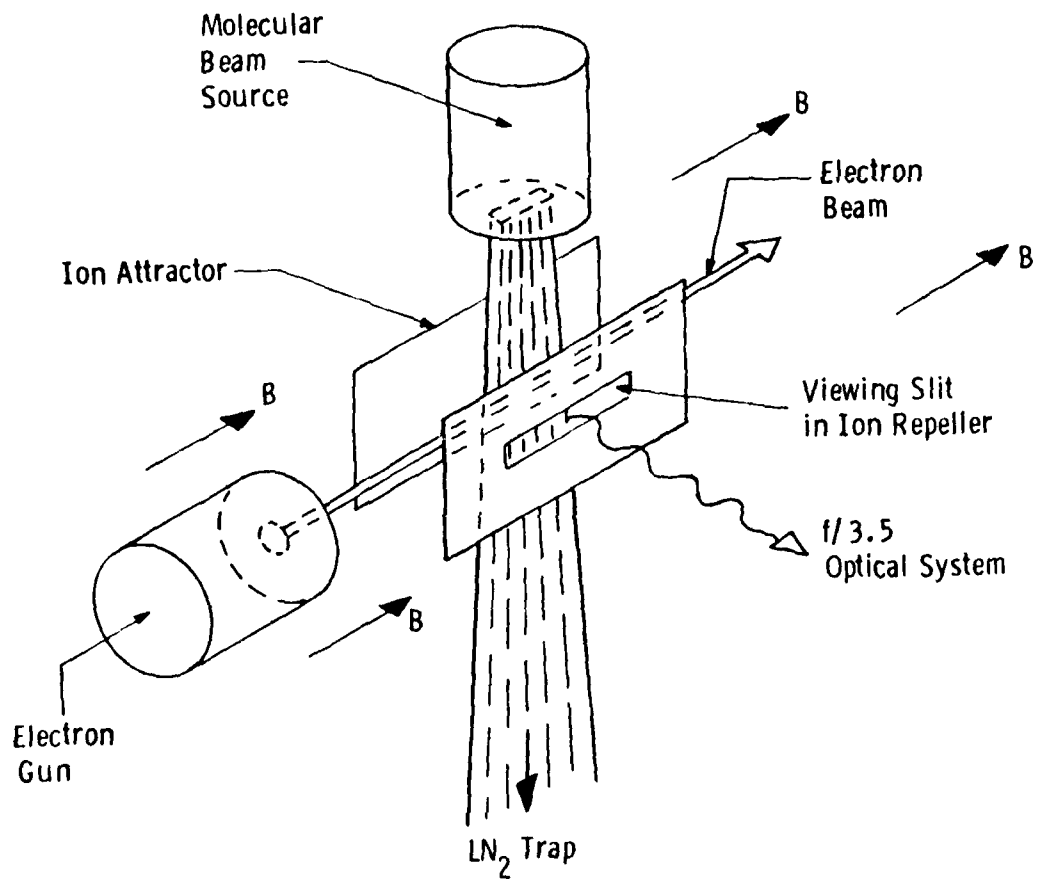


Fig. 1 Schematic of crossed beam system

Dwg. 7757A3R

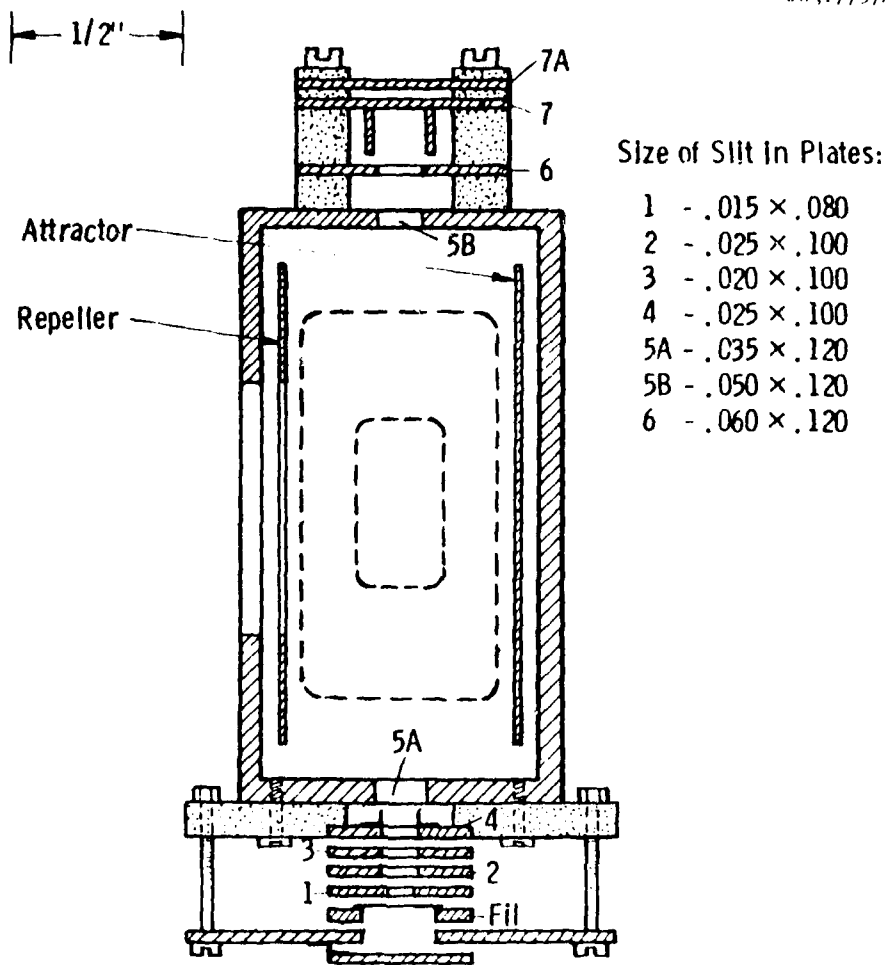


Fig. 2 Horizontal section of collision chamber

Dwg. 7757A39

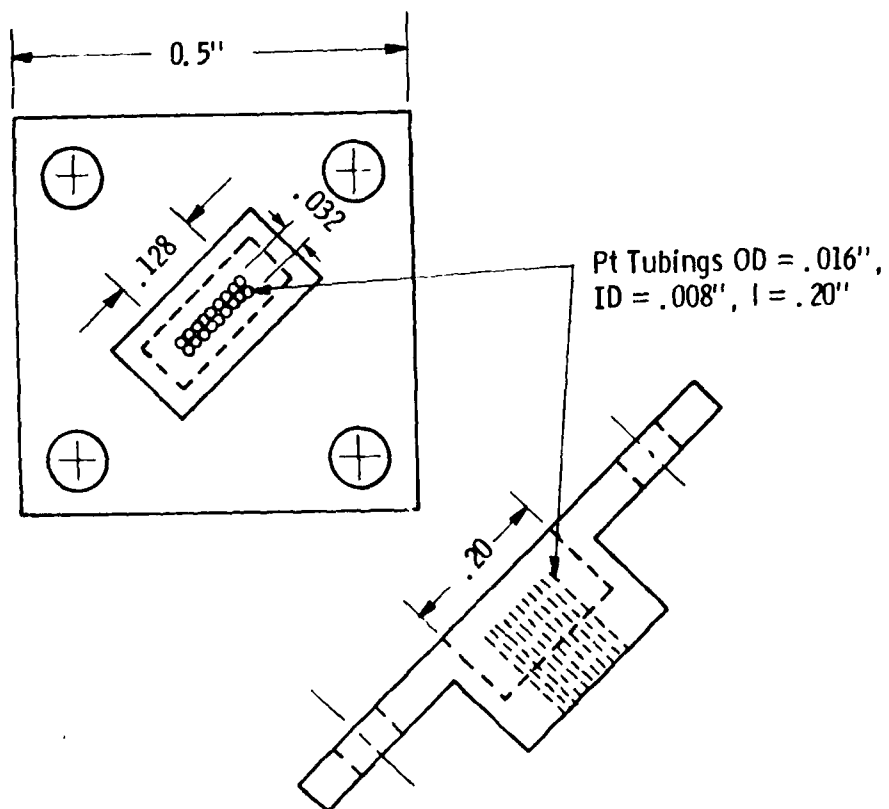


Fig. 3 Molecular beam head

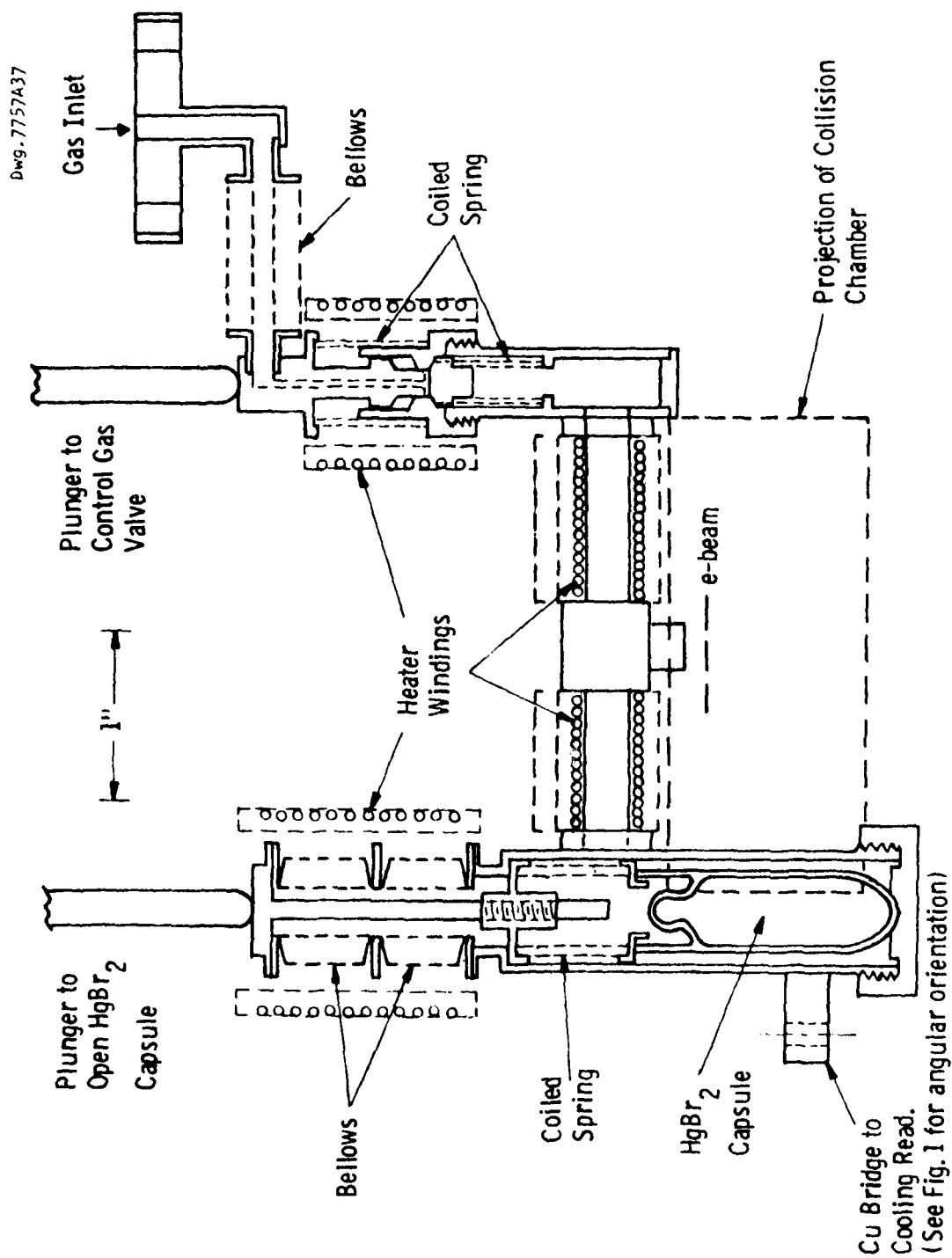


Fig. 4 HgBr_2 reservoir, molecular beam head and valve control system for permanent and reference gases

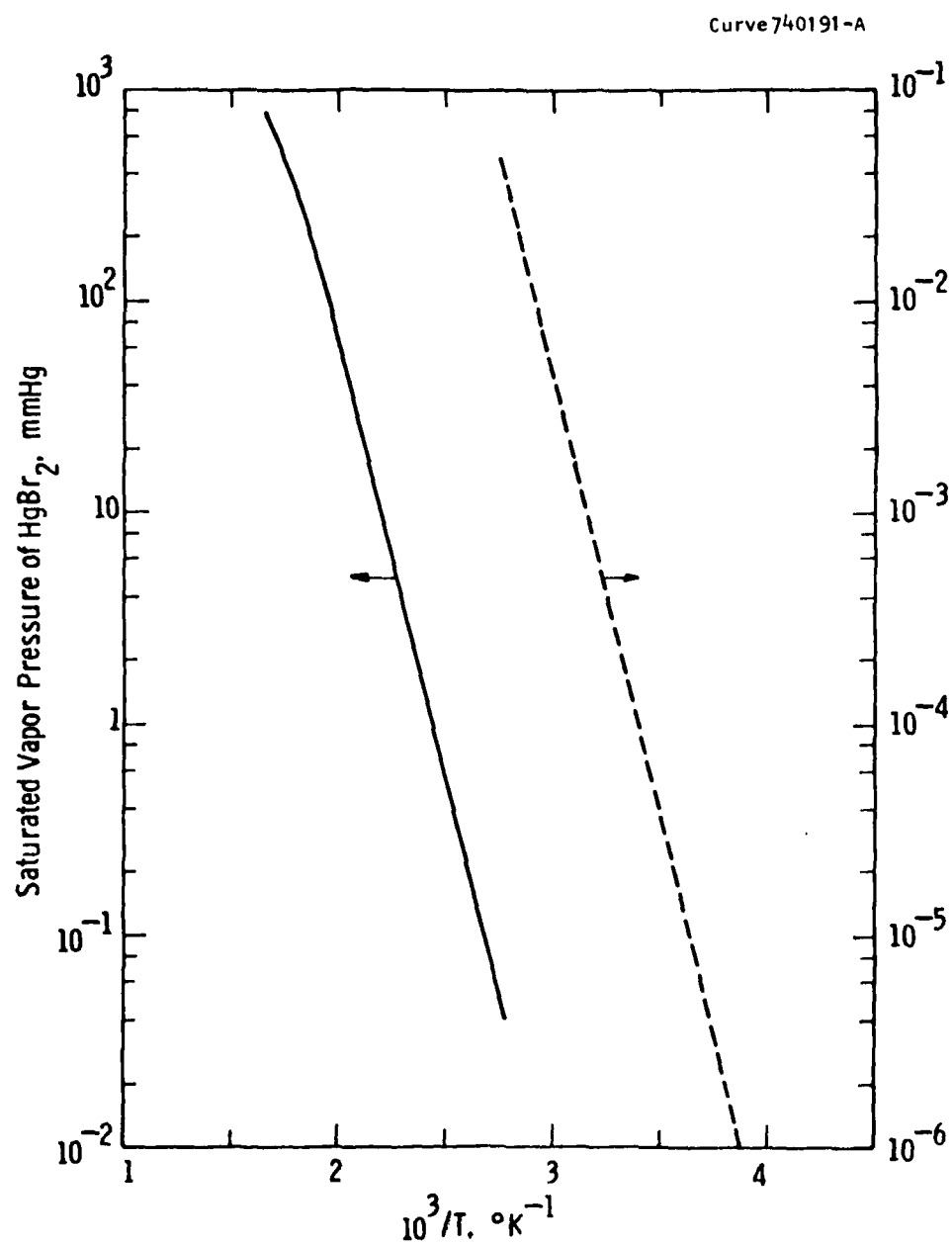


Fig. 5 HgBr_2 vapor pressure curve as a function of inverse temperature

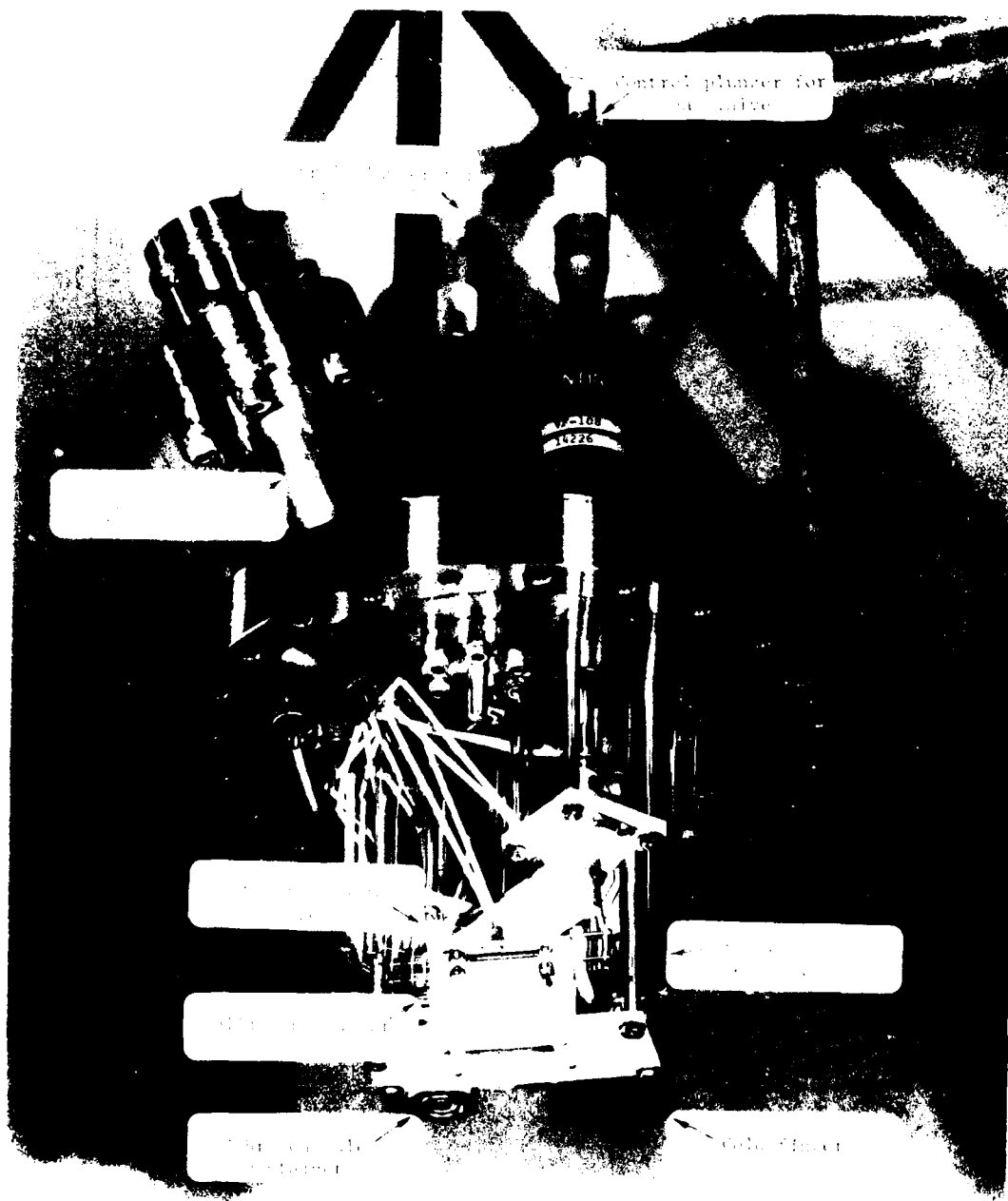


Fig. 6 Photograph of apparatus

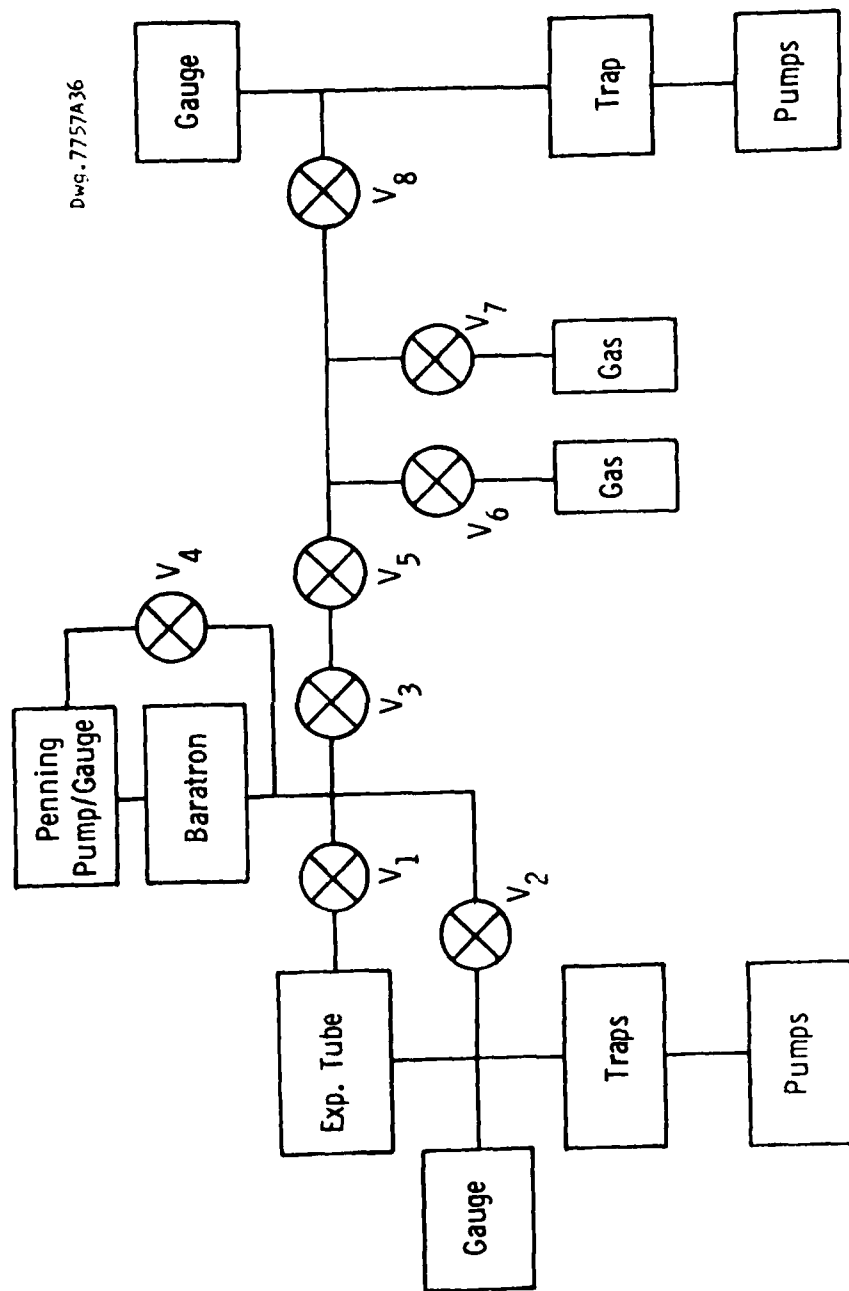


Fig. 7 Schematic diagram of gas handling and pumping system

Dwg. 7770A89

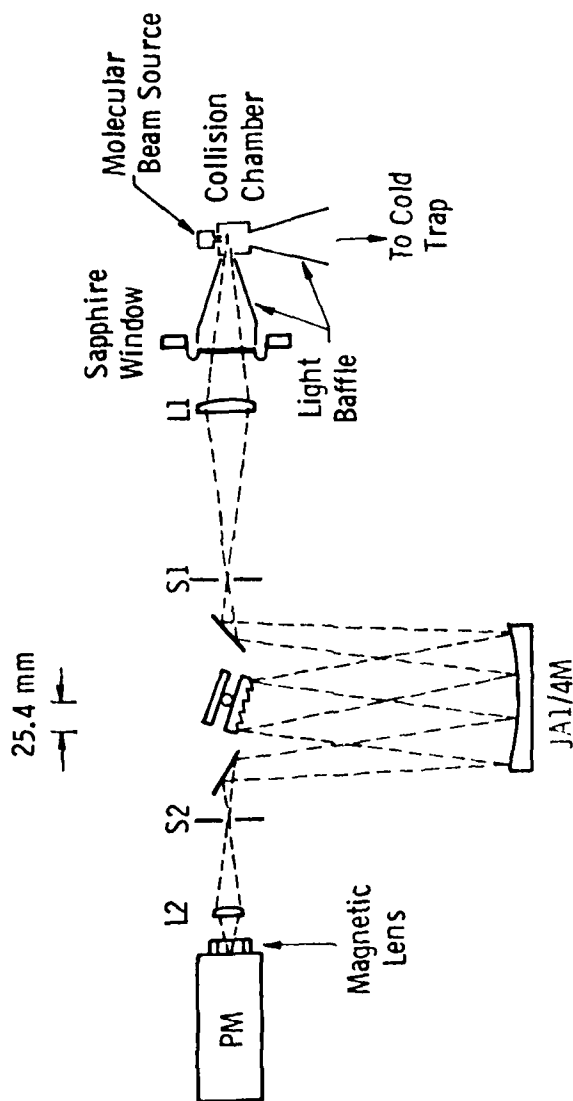


Fig. 8 Schematic diagram of optical system. L1 and L2 are quartz lenses, S1 and S2 are entrance and exit slits of the Jarrell-Ash 0.25 meter Ebert monochromator. Two light baffles (out of five) shown are designed to cut down scattered light from heated filament entering the optical system.

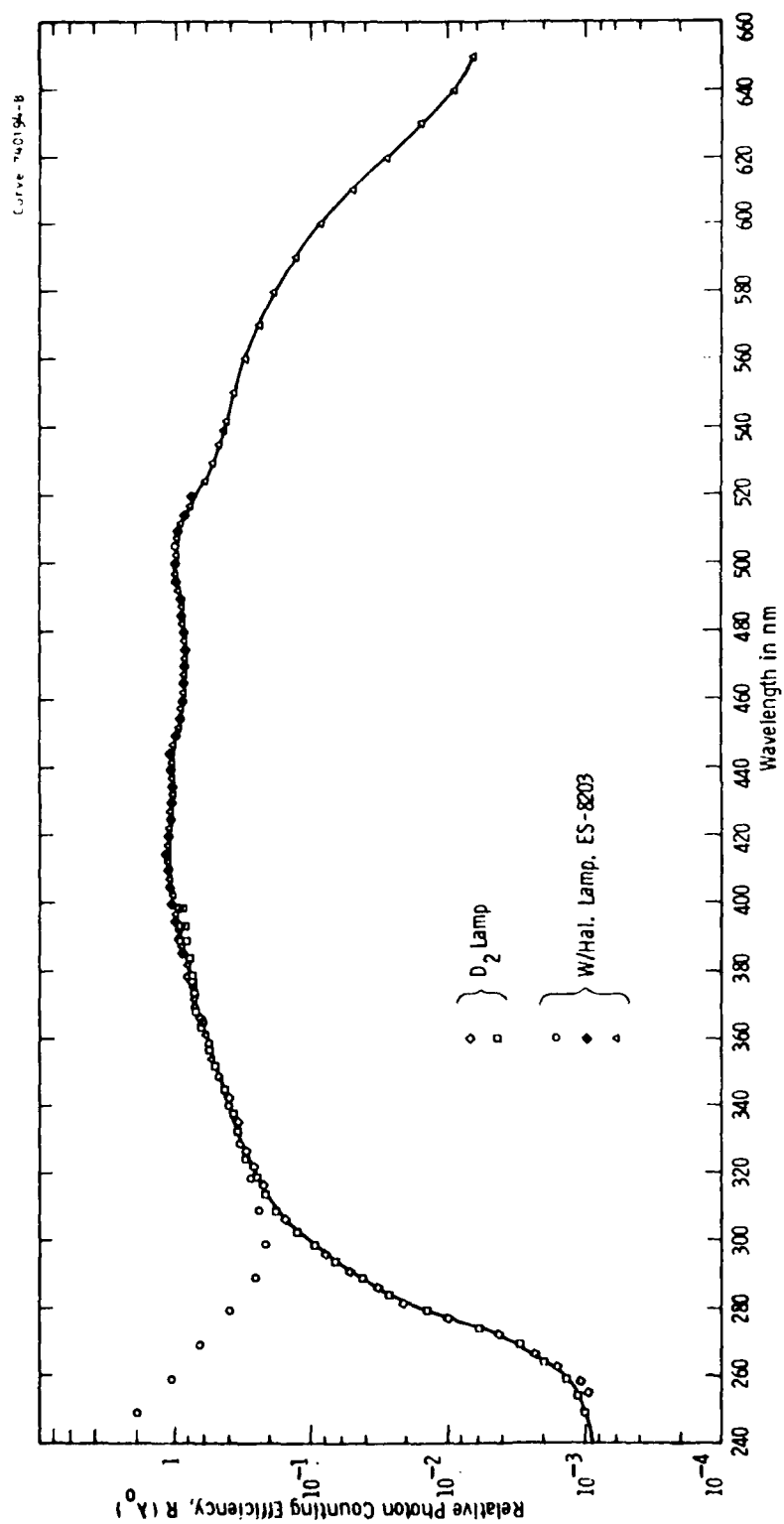


Fig. 9 Relative photon counting efficiency $R(\lambda_0)$ of the optical system as a function of wavelength determined with deuterium discharge and tungsten halogen standard lamps.

Curve 740192-A

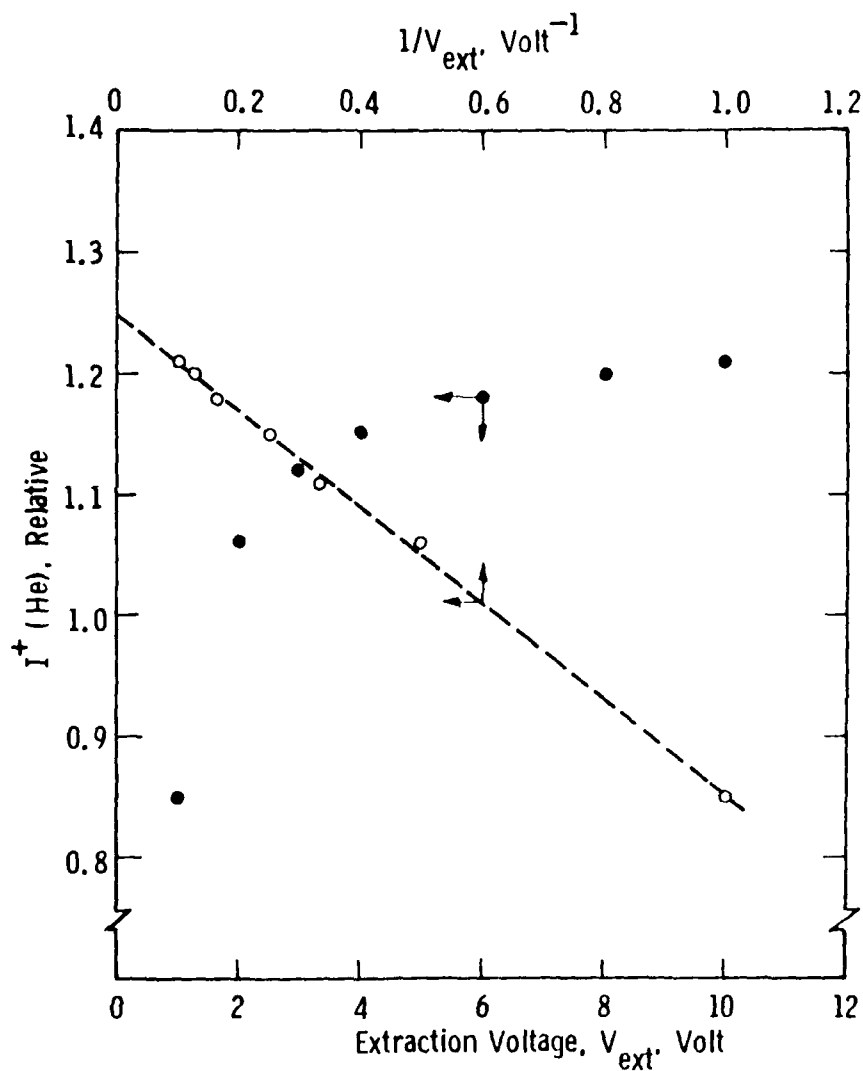


Fig. 10 Helium positive ion saturation current I^+ curve as a function of extraction voltage V_{ext} (solid points) applied to the pair "attractor" and "repeller" electrodes. The open circles are plots of I^+ versus V_{ext}^{-1} .

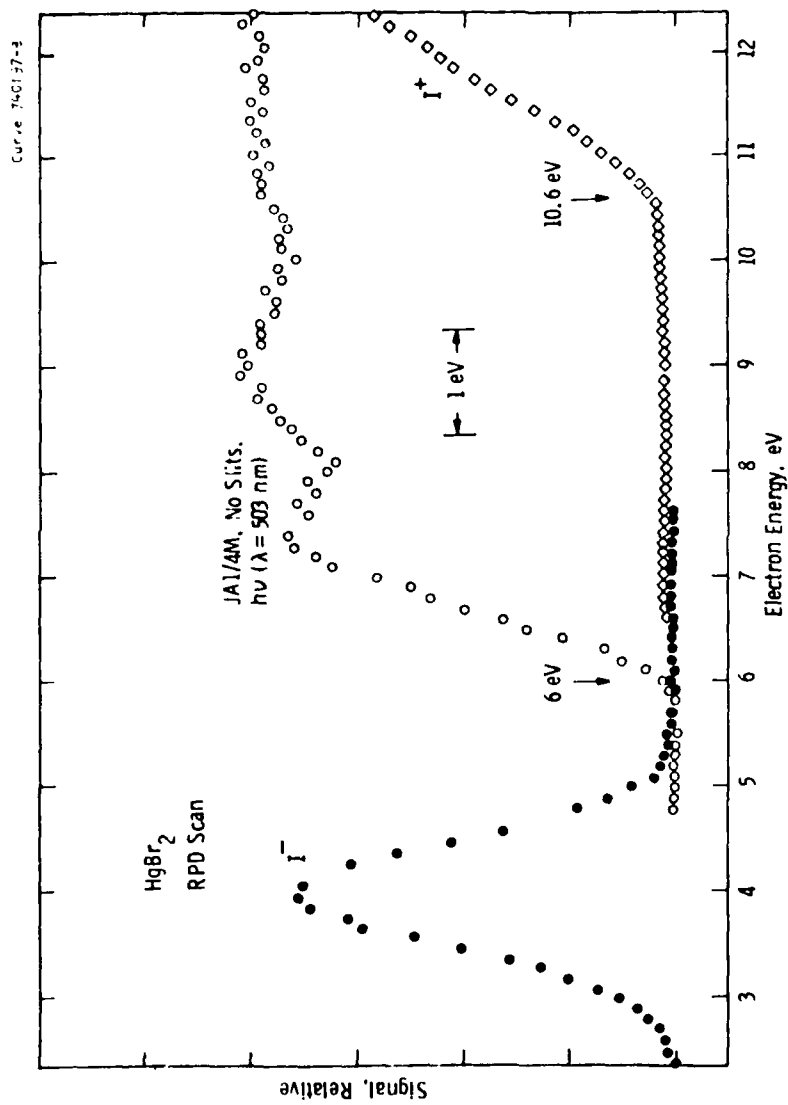


Fig. 11 HgBr(B-X) band fluorescence raw data at 502 nm as a function of electron energy ϵ . The slit width of the Jarrell-Ash 0.25 meter spectrometer is wide open. In this figure we also show the positive ion current I^+ and the negative ion current I^- collected by the "repeller" and "attractor" electrodes, respectively. Except shapes and positions, there is no significance of the relative magnitude of these three sets of data.

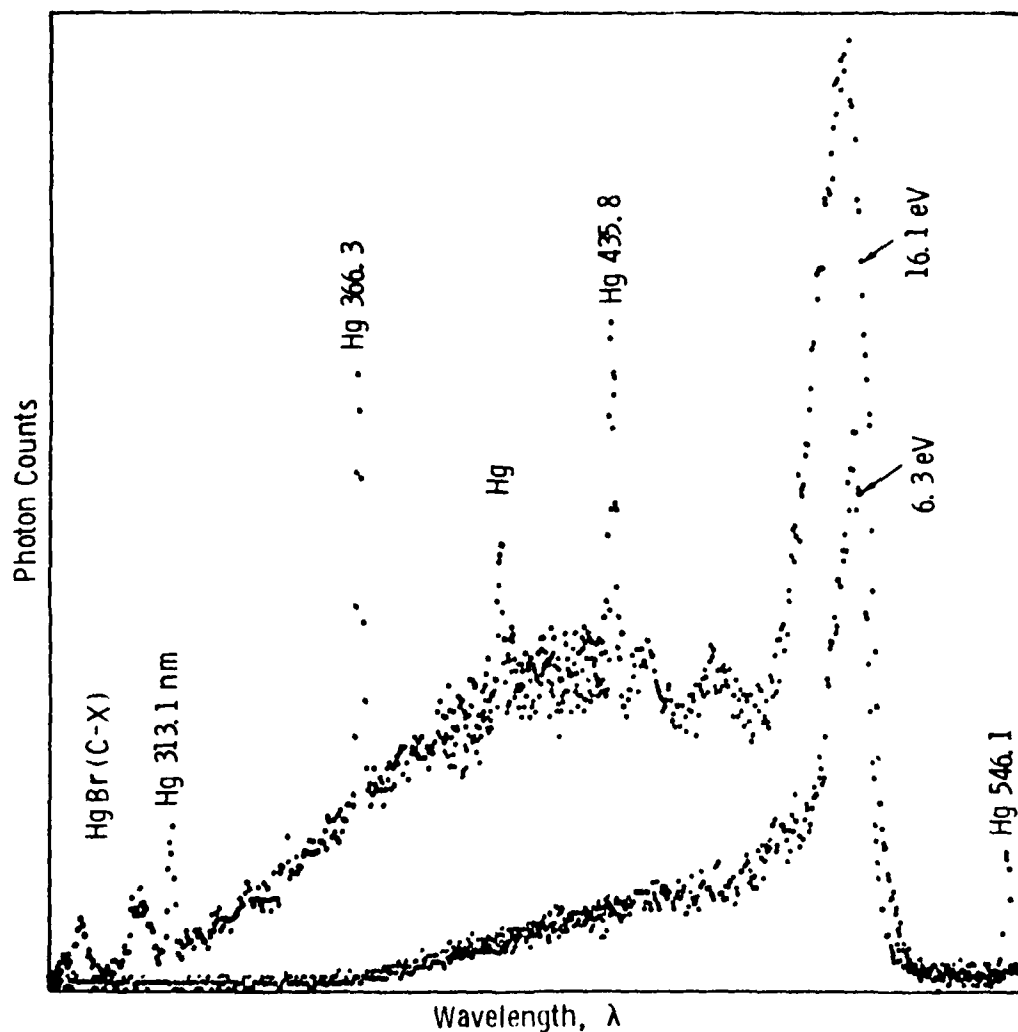


Fig. 12 Photon counts of HgBr(B-X) fluorescence as a function of wavelength λ at electron energy $\epsilon = 6.3$ and 16.1 eV. The mercury lines at 313.1, 366.3, 435.8 and 546.1 nm are used for wavelength calibrations. The HgBr(C-X) fluorescence below Hg 313.1 nm is clearly observable at $\epsilon = 16.1$ eV.

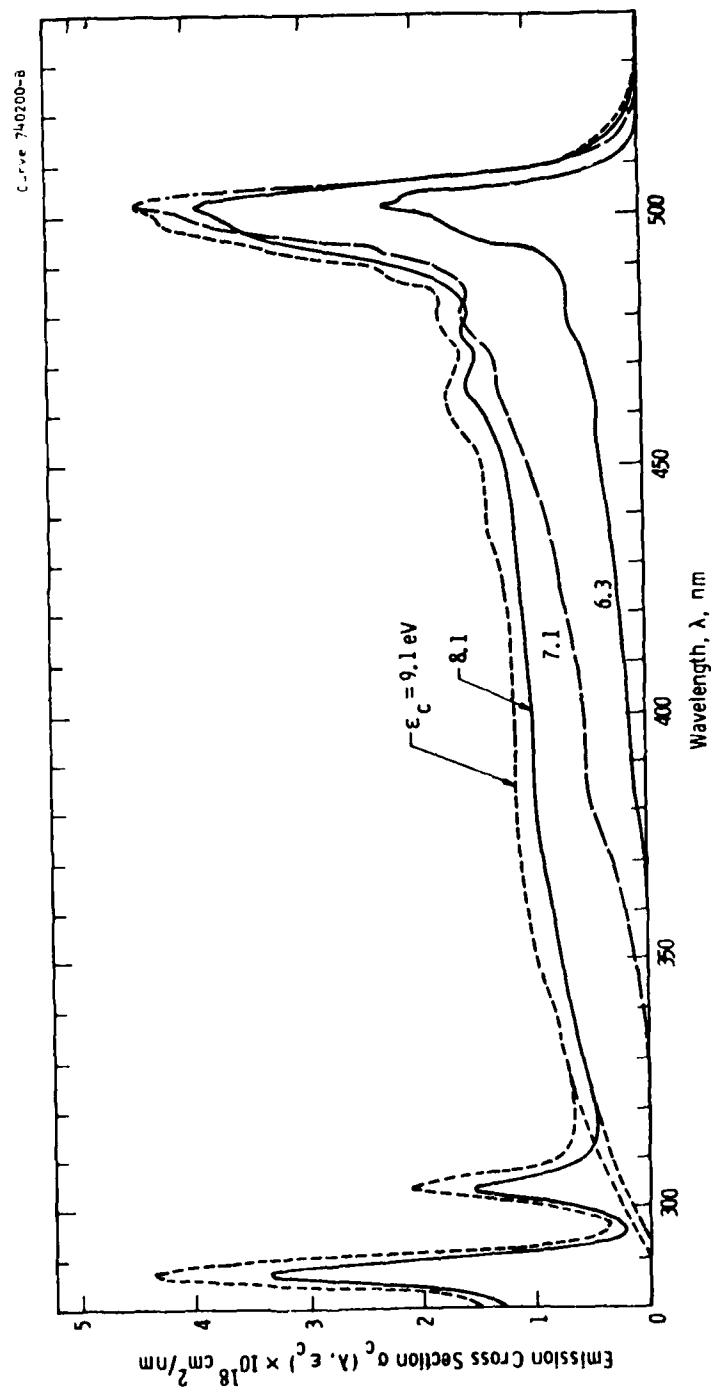


Fig. 13 Wavelength resolved emission cross section $\sigma_c(\lambda, \epsilon_c)$ of $\text{HgBr}^*(\text{B-X})$ for electron energies $\epsilon_c = 6.3, 7.1, 8.1$ and 9.1 eV .

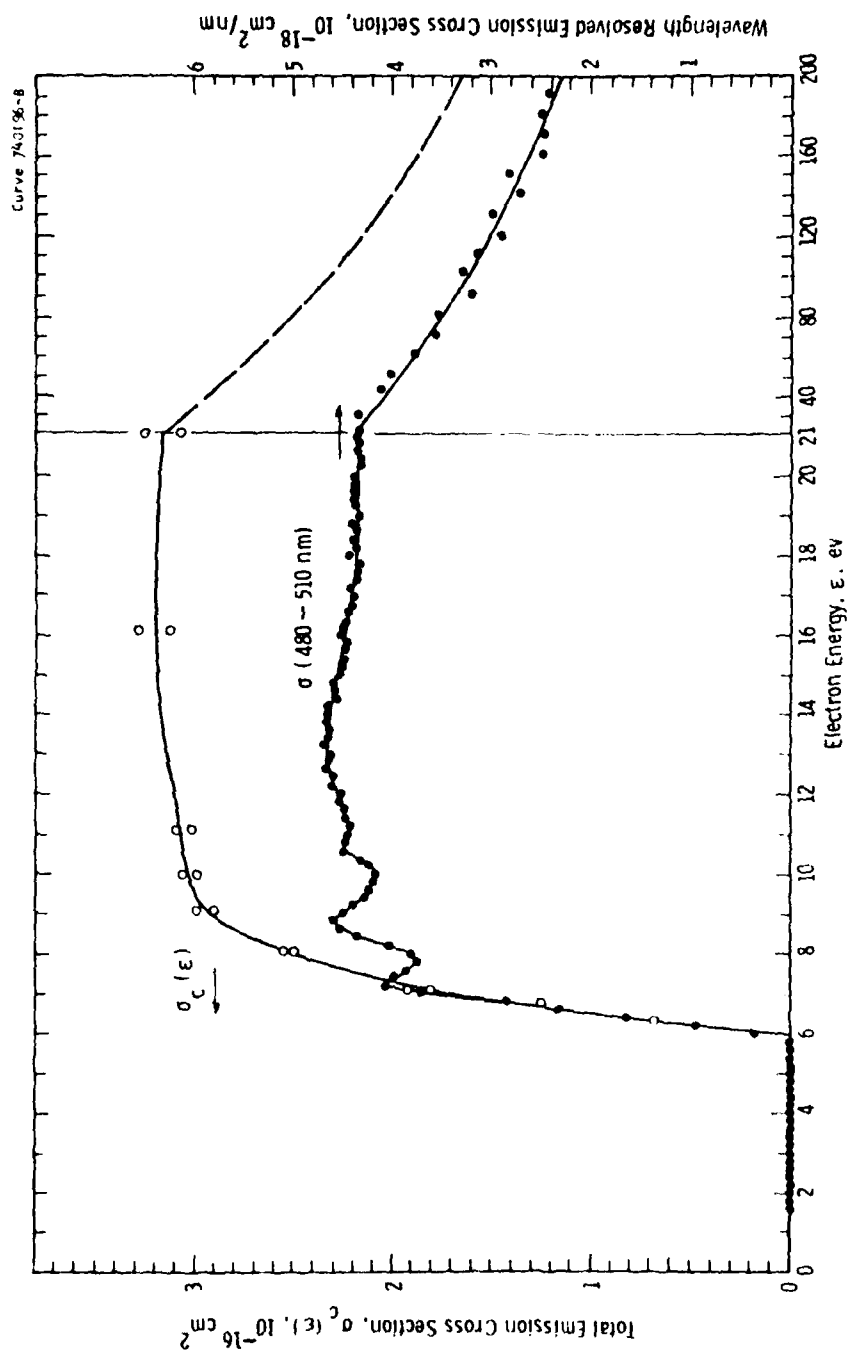


Fig. 14 A linear plot of total emission cross section $\sigma_c(\epsilon)$ of $\text{HgBr}^*(\text{B-X})$ versus electron energy ϵ . In this figure we also present a wavelength resolved emission cross section as a function of electron energy, the pass band of the optical system is 480-510 nm (FWHM) centered at 495 nm.

Curve 74072b-8

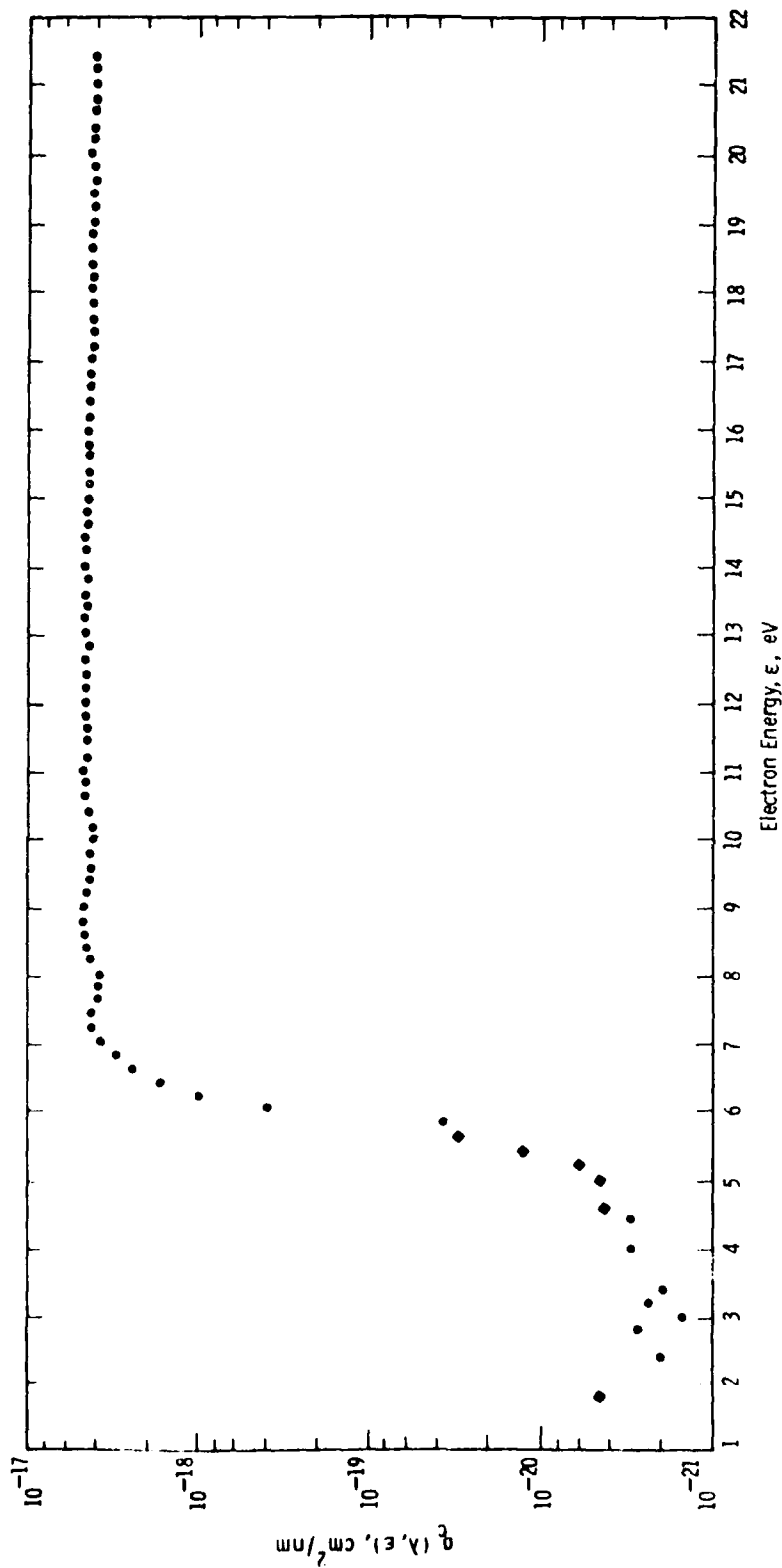


Fig. 15 A semi-log plot of wavelength resolved emission cross section versus electron energy. The Jarrell-Ash 0.25 meter Ebert spectrometer was operated without slits and the grating was set at 495 nm. The measured instrument function has a full width at half maximum of 30 nm.

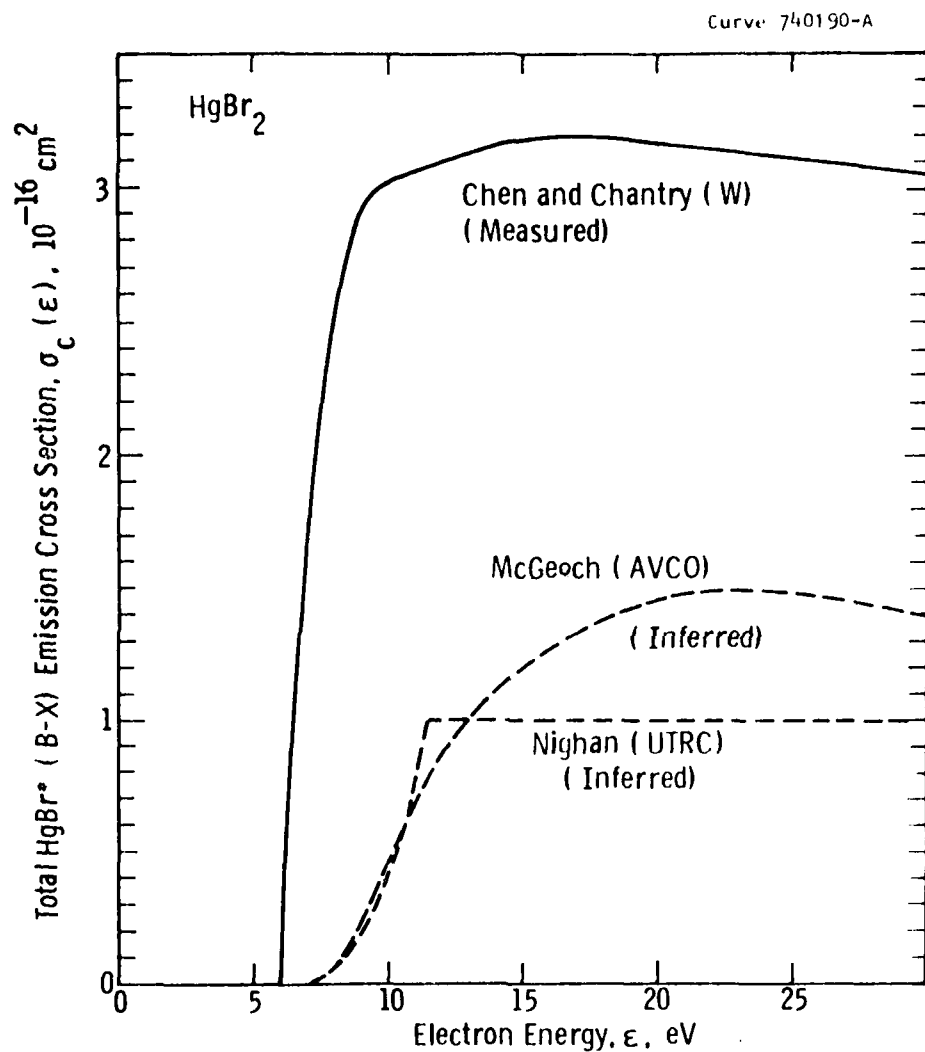


Fig. 16 Comparison of McGeoch's (AVCO) and Nighan's (UTRC) inferred $\text{HgBr}^*(\text{B-X})$ emission cross sections to the present measured one .

DATE
FILMED

11-82

DTIC